Discovery of novel microRNA regulators of ribosome biogenesis

Carson J. Bryant [a], Mason A. McCool [a], Gabriela T. Rosado-González [a], Laura Abriola [b], Yulia V. Surovtseva [b], Susan J. Baserga [a, c, d]

[a] Department of Molecular Biophysics and Biochemistry, Yale School of Medicine, New Haven, CT, USA.

[b] Yale Center for Molecular Discovery, Yale University, West Haven, CT, USA.

[c] Department of Genetics, Yale School of Medicine, New Haven, CT, USA.

[d] Department of Therapeutic Radiology, Yale School of Medicine, New Haven, CT, USA.

Address correspondence to Susan J. Baserga (Molecular Biophysics and Biochemistry, PO Box 208024, 333 Cedar Street, New Haven, CT 06520-8024, USA; +1-203-785-4618, susan.baserga@yale.edu).

Abstract

While microRNAs and other non-coding RNAs are the next frontier of novel regulators of mammalian ribosome biogenesis (RB), a systematic exploration of microRNA-mediated RB regulation has not yet been undertaken. We carried out a high-content screen in MCF10A cells for changes in nucleolar number using a library of 2,603 mature human microRNA mimics. Following a secondary screen for nucleolar rRNA biogenesis inhibition, we identified 72 novel microRNA negative regulators of RB after stringent hit calling. Hits were enriched for mRNA targets encoding proteins with nucleolar localization or functions in cell cycle regulation. Rigorous selection and validation of a subset of 15 microRNA hits unexpectedly revealed that most of them caused dysregulated pre-rRNA processing, elucidating a novel role for microRNAs in RB regulation. Almost all 15 hits impaired global protein synthesis and upregulated *CDKN1A* (*p21*) levels, but caused diverse effects on RNA Polymerase 1 (RNAP1) transcription and TP53 protein levels. We defined *RPS28* as a direct target of the MIR-28 siblings, hsa-miR-28-5p and hsa-miR-708-5p, which caused a severe pre-18S pre-rRNA processing defect, and uncovered SPRR3's novel role in promoting RNAP1 transcription. Our work illuminates novel microRNA attenuators of RB, forging a promising new path for microRNA mimic chemotherapeutics.

Graphical Abstract

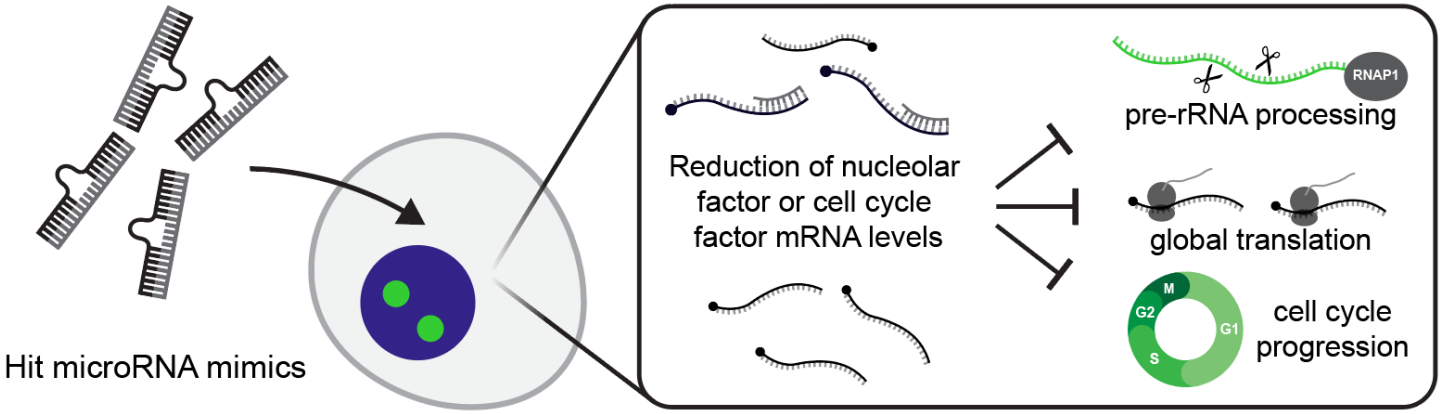

Introduction

Ribosome biogenesis (RB) is the complex, essential process by which mature small and large ribosomal subunits are produced in all living organisms. Eukaryotes partition many RB steps into the nucleolus, a phase-separated membraneless organelle within the enveloped nucleus (1-3). In human cells, three of the four mature ribosomal RNAs (rRNAs), the 18S, 5.8S, and 28S rRNAs, are synthesized in the nucleolus as components of the polycistronic 47S primary pre-rRNA precursor transcript from tandem ribosomal DNA (rDNA) repeats by RNA Polymerase 1 (RNAP1) (4). The 5S rRNA is separately transcribed in the nucleus by RNA Polymerase 3 (RNAP3) (5,6). A myriad of ribosome assembly factors (AFs) execute endo- and exonucleolytic pre-rRNA processing and modification events to liberate the mature rRNAs from the 47S transcript, forming the small 40S and large 60S ribosomal subunits (7-10). AFs also facilitate the binding of structurally-constitutive ribosomal proteins (RPs) and the folding of the maturing subunits at the macromolecular scale (11-16). Defects in RB can trigger the nucleolar stress response during which labile members of the 5S RNP including RPL5 (uL18) or RPL11 (uL5) bind and sequester the TP53-specific E3 ligase MDM2, effectively stabilizing TP53 levels and leading to *CDKN1A* (*p21*) induction, cell cycle arrest, and apoptosis (17-19). At the organismal level, nucleolar stress resulting from RB defects can cause a class of rare human diseases called ribosomopathies (19-22). Furthermore, cancer initiation and progression are strongly linked to aberrant RB (23-29).

MicroRNAs comprise a class of non-coding (nc)RNAs of approximately 22 nt which can base pair with messenger (m)RNAs to post-transcriptionally reduce transcript stability or translation efficiency, acting as “sculptors of the transcriptome” to fine-tune gene expression (30-32). Like RB, microRNAs play critical roles in mediating human development, health, and disease including cancer (33,34). How microRNAs regulate RB has yet to be explored systematically at the experimental level, yet there are some intriguing links between them. A handful of microRNAs have been experimentally

described to affect RB subprocesses including RNAP1 transcription, 60S assembly, and RP gene transcription (35). Consistent with this, the microRNA biogenesis factors Drosha and Dicer are required for 28S and 5.8S maturation (36). AGO2, the microRNA-binding component of the active RISC complex (32), has been found in the nucleolus (37) along with several microRNAs (38-40), though their precise biological function there remains unclear. Computational analysis has implicated microRNA-mediated control of RPs as a key potentiator of RB activity and disease progression (41), thereby necessitating additional *in vivo* experiments. Software packages have made some inroads towards accurate prediction of microRNA targets (42,43) or functions (44) although abundant false positives limit their utility (41,45). The limited amount of direct experimental evidence that microRNAs are involved in RB represents a significant gap in our understanding of the layers of regulation of nucleolar function in human cells.

Previously, our laboratory established an effective and robust screening platform to identify novel regulators of RB by exploiting the close relationship between nucleolar number and function (46,47). Importantly, we discovered that either a decrease or increase in nucleolar number from 2-4 nucleoli per nucleus following genetic perturbation is strongly predictive of aberrant RB in human MCF10A breast epithelial cells. Our high-content screening platform leverages changes in nucleolar number to identify putative novel regulators of RB. For these genome-wide siRNA screens, we reverse-transfected MCF10A cells with an arrayed library of siRNAs for 72 h. Following treatment, we fixed and stained the cells for the nucleus and the nucleolus, conducted automated imaging, and used a custom CellProfiler pipeline to count the number of nucleoli per nucleus on a per-cell basis. Screening statistics were robust, with routine Z' factors above 0.5. Together, our laboratory's previous RNAi-based nucleolar number screening campaigns have successfully identified over 250 novel protein-coding regulators of RB (46,47).

To date, no holistic, unbiased discovery campaign for microRNAs functioning in RB regulation has been conducted, and the full complement of microRNAs affecting RB remains poorly understood. We previously hypothesized that microRNAs may be a key, underappreciated conduit linking biochemical RB defects to the pathogenesis of diseases like ribosomopathies and cancer (35). To discover novel microRNAs negatively regulating RB, we conducted a high-content screen for changes in nucleolar number following microRNA mimic overexpression in human MCF10A cells. High-throughput screens using microRNA mimics have previously revealed mechanistic insight into microRNA-mediated regulation dynamics during cellular proliferation and signaling (48,49), cardiac regeneration (50), viral infection (51), and cancer (52,53).

Here, we identify 72 high-confidence mature human microRNA hits that disrupt RB, which are enriched for mRNA targets involved in cell cycle regulation, cellular proliferation, and localization within the nucleolus. We validate the roles of a subset of 15 hits in RB subprocesses including pre-

rRNA transcription, pre-rRNA processing, and global protein synthesis. For the first time, we directly define the abilities of 12 microRNAs to inhibit pre-rRNA processing. Our work reveals that the MIR-28 family members, hsa-miR-28-5p and hsa-miR-708-5p, are strong inhibitors of pre-40S pre-rRNA processing by way of *RPS28* downregulation. The MIR-28 family also targets *SPRR3*, an understudied oncogene whose depletion causes a decrease in nucleolar number, and which we show is essential for pre-rRNA transcription and global protein synthesis, but not for pre-rRNA processing. Our screen's results underscore the broad potential of microRNAs to dysregulate RB, and raise new questions regarding the extent to which microRNAs may connect RB and disease.

Materials and Methods

Cell lines and culture conditions

Human MCF10A breast epithelial cells (ATCC CRL-10317) were cultured in DMEM/F-12 (Gibco 11330032) with 5% horse serum (Gibco 16050122), 10 µg/mL insulin (MilliporeSigma I1882), 0.5 µg/mL hydrocortisone (MilliporeSigma H0135), 20 ng/mL epidermal growth factor (Peprotech AF-100-15), and 100 ng/mL cholera toxin (MilliporeSigma C8052). Cells were incubated at 37 °C in a humidified atmosphere with 5% CO2.

Chemical reagents

BMH-21 (Sigma-Aldrich SML1183; CAS 896705-16-1) was diluted to a working stock concentration of 50 µM in DMSO for direct dosing of cells in 384-well plates.

RNAi depletion and microRNA expression by reverse-transfection

RNAi depletion was conducted in MCF10A cells as previously reported (46,47,54). Briefly, MCF10A cells were reverse-transfected into an arrayed 384-well plate library containing small interfering RNA (siRNA) or miRIDIAN microRNA mimic constructs (Horizon Discovery, **Supplementary Tables 1-3**) using Opti-MEM (Gibco 31985070) and Lipofectamine RNAiMAX transfection reagent (Invitrogen 13778150). Assay-ready plates containing 10 µL of 100 nM microRNA mimics resuspended in 1X siRNA buffer (Horizon Discovery B-002000-UB-100) were prepared from master library 384-well plates (Horizon Discovery, 0.1 nmol scale) and stored at -80 C. Plates were prepared with control siRNAs (siNT, siNOL11, siKIF11, or siPOLR1A) for reverse-transfection at a final 20 nM siRNA/microRNA mimic concentration as described (54), at a seeding density of 3000 MCF10A cells/well. The miRIDIAN microRNA hairpin inhibitor library (Horizon Discovery, **Supplementary**

Table 4) was screened using the same protocol. siRNA deconvolution for SPRR3 was conducted as previously reported (55).

5-ethynyl uridine labeling; staining and high-content imaging

5-ethynyl uridine (5-EU; ClickChemistryTools 1261-100, CAS 69075-42-9) was used to label cells at a 1 mM final concentration. Staining, click chemistry, and high-content imaging were performed as previously described (54).

CellProfiler pipeline and data analysis

Image analysis and data processing were conducted using a custom pipeline for CellProfiler 3.1.9 as previously described (46,47,54,56,57). Strictly-standardized mean difference (SSMD) values were calculated from plate-adjusted one-nucleolus or 5+ nucleoli percent effect values using the uniformly minimal variance unbiased estimate (UMVUE), equation A5 in (58). Data from the primary or secondary screen were averaged in JMP and graphed with JMP or GraphPad Prism 8 (GraphPad Software).

MCF10A RNA expression dataset

Deposited reads from four RNAseq experiments from MCF10A cells quantifying transcript levels without treatment (negative control conditions; see table below) were re-analyzed using Partek Flow. Reads were aligned to the hg38 genome with HISAT2 2.1.0 and quantified using the Ensembl Transcripts version 99 annotation with the Partek E/M algorithm module. Normalized transcripts per million (zTPM) for genes in each experiment was calculated in R as described (59). For each dataset, a given gene was categorized as expressed if its zTPM was greater than -3, as described in (59) (**Supplementary Table 5**).

BioProject accession	GEO samples used	Reference
PRJNA290557	GSM1829628	(60)
PRJNA384982	GSM2593351, GSM2593352, GSM2593353	(61)
PRJNA530983	GSM3711368, GSM3711369	N/A
PRJNA647393	GSM4667014, GSM4667015, GSM4667016	(62)

Nucleolar protein metadatabase

Three nucleolar protein databases were merged to create a nucleolar protein metadatabase. The Human Protein Atlas subcellular localization database (v. 20.0) (63, proteinatlas.org) containing 1350 unique nucleolar proteins was retrieved, and HGNC gene names were updated based on Ensembl Gene ID using BioMart. Proteins labeled with the GO terms “Nucleoli”, “Nucleoli fibrillar center”, or

"Nucleoli rim" were considered to be nucleolar. The T-cell nucleolar proteome (64) containing 880 unique nucleolar proteins was retrieved, and HGNC gene names were updated based on NCBI Entrez Gene ID using BioMart. An archived copy of NOPdb 3.0 (65) containing 2242 unique nucleolar proteins was retrieved, and HGNC gene names were updated based on International Protein Index (IPI) ID using the latest IPI database release (v. 3.87) and BioMart. The three databases were merged on updated HGNC name, resulting in a metadatabase of 3490 unique nucleolar proteins (**Supplementary Table 6**).

Bioinformatic target enrichment analysis

TarBase 8 (66) was utilized to identify experimentally-validated microRNA:mRNA interactions. Genes were filtered for the *Homo sapiens* species, for true positive microRNA:mRNA interactions, and for interactions where the microRNA caused reduced levels of the mRNA. Next, genes were annotated with zTPM expression data from the MCF10A expression dataset (see above), for nucleolar localization using the nucleolar protein metadatabase (see above), and 89 cytosolic RP genes were labeled based on HGNC gene groups (35 "S ribosomal proteins", HGNC gene group 728; 54 "L ribosomal proteins", HGNC gene group 729). The number of genes targeted by each microRNA was calculated in JMP, and confirmed hit microRNAs were labeled. Subset tabulations were also carried out to determine the number of genes coding for nucleolar proteins targeted by each microRNA, and the number of genes coding for RPs targeted by each microRNA. Mean and median values for each category were calculated with JMP for hit microRNAs and non-hit microRNAs. Conversely, the number of microRNAs targeting each gene was also calculated with JMP, and all 262 genes targeted by 5 or more microRNA hits were analyzed for enrichment using Enrichr (67-69) (**Supplementary Table 7**).

RNA isolation following RNAi transfection

MCF10A cells were seeded at 100,000 cells per well in 2 mL of media in 6-well plates and incubated at 37 °C for 24 h. Cells were transfected with 30 nM siRNAs or microRNA mimics using Lipofectamine RNAiMAX (Invitrogen 13778-150) and Opti-MEM (Gibco 31985070) per manufacturer's instructions for 72 h. Cells were washed with 1X PBS, then collected with 1 mL of TRIzol reagent (Invitrogen 15596026). Total RNA was purified following the manufacturer's protocol.

PolyA+ RNAseq following overexpression of hsa-miR-28-5p or hsa-miR-708-5p

MCF10A cells were treated with siNT, hsa-miR-28-5p, or hsa-miR-708-5p, and RNA was isolated as above. One µg of total RNA was resuspended in nuclease-free H_2O and submitted to the Yale Center for Genomic Analysis (West Haven, CT) for polyA+ library preparation and sequencing. All samples

had an RNA Integrity Number (RIN) of at least 9.6. 35-50 million 100 bp paired-end reads were collected per sample using a NovaSeq 6000 Sequencing System (Illumina). RNAseq was conducted in biological triplicate. Partek Flow was used to process, align, and quantify reads. Reads were trimmed of adapters, then aligned to the hg38 genome with HISAT2 2.1.0. Reads were quantified using the RefSeq Transcripts version 93 annotation with the Partek E/M algorithm module. Differential expression analysis was conducted with DESeq2 (70). Raw reads are available on NCBI under BioProject accession PRJNA919164 and processed data are summarized in **Supplementary Table 8**.

Analysis of RNA transcript levels by RT-qPCR

MCF10A cells were treated with control siRNAs or microRNA mimics, and RNA was isolated as above. cDNA was synthesized from 1 µg total input RNA using iScript™ gDNA Clear cDNA Synthesis Kit (Bio-Rad 1725035). In a qPCR plate (Bio-Rad MLL9601), 1 µL of cDNA was dispensed, followed by 19 µL of a qPCR master mix containing iTaq Universal SYBR Green Supermix (Bio-Rad 1725121), 500 nM forward primer, 500 nM reverse primer, and water. The plate was briefly centrifuged and assayed using a Bio-Rad CFX96 Touch Real-Time PCR Detection System. Amplification parameters were: initial denaturation 95 ºC for 30 s; 40 cycles 95 ºC denaturation for 15 s, 60 ºC annealing and extension for 30 s. Melt curve analysis parameters were: 60 ºC to 94.8 ºC in 0.3 ºC increment. Data analysis was completed using the comparative C_T method ($\Delta\Delta C_T$) using 7SL RNA as an internal loading control.

Target RNA	Forward primer (5' → 3')	Reverse primer (5' → 3')	Ref.
45S pre-rRNA	GAACGGTGGTGTGTCGTTC	CGTCTCGTCTCGTCTCACTC	(71)
7SL RNA	ATCGGGTGTCCGCACTAAGTT	CAGCACGGGAGTTTTGACCT	(72)
CDKN1A (*p21*)	TGGAGACTCTCAGGGTCGAAA	GGCGTTTGGAGTGGTAGAAATC	(73)
RPS28	GGTCTGTCACAGTCTGCTCC	CATCTCAGTTACGTGTGGCG	(74)
SPRR3	AGCAGGTCCAGCATCCTTTGA	CTCCTTGGTTGTGGGAACAAAT	(75)

Analysis of mature rRNAs

MCF10A cells were treated with control siRNAs or microRNA mimics, and RNA was isolated as above. One µg of total RNA was resuspended in nuclease-free H_2O and submitted to the Yale Center for Genomic Analysis for electropherogram analysis. Each experiment was conducted with either a Bioanalyzer 2100 or a Fragment Analyzer 5300 (Agilent). Mature rRNA ratios and mature rRNA relative peak areas were taken from the output reports. The data were graphed and analyzed by ANOVA followed by Holm-Šídák post-hoc testing in GraphPad Prism.

Northern blot analysis of pre-rRNA processing

MCF10A cells were treated with siRNAs or microRNA mimics, and RNA was isolated as above. Northern blots were performed using 3 µg of total RNA as published (46,47), and were performed in at least biological triplicate. Blots were quantified with Image Lab 6.0.1 (Bio-Rad). RAMP [Ratio Analysis of Multiple Precursors, (76)] ratios were calculated in Microsoft Excel, and heatmaps were made using the mean $\log_2$ RAMP ratio for each treatment relative to siNT in GraphPad Prism. The following DNA oligonucleotides were radiolabeled for blotting:

Probe name	Probe sequence (5' → 3')	Ref.
P3 (ITS1)	AAGGGGTCTTTAAACCTCCGCGCCGGAACGCGCTAGGTAC	(46)
P4 (ITS2)	CGGGAACTCGGCCCGAGCCGGCTCTCTCTTTCCCTCTCCG	(46)

Dual-luciferase assay for RNAP1 promoter activity

MCF10A cells were seeded at 30,000 cells per well in 1 mL of media in 12-well plates and incubated at 37 °C for 24 h. Cells were transfected with 30 nM siRNAs or microRNA mimics as above for 48 h. Cells were then transfected with 1 µg of pHrD-IRES-Fluc and 1 ng of CMV-Rluc reporter plasmids (55) using Lipofectamine 3000 (Invitrogen L3000015). Concurrently, cells were treated with 3.5 µL of DMSO vehicle or 300 µM BMH-21, to achieve a final concentration of 1 µM BMH-21. After another 24 h, treated cells were washed once with 1X PBS and lysed with 250 µL of 1X Passive Lysis Buffer (Promega E1941) at room temperature for at least 30 minutes. In a solid white 96-well plate (Greiner Bio-One 655074), 20 µL of lysate from each sample was dispensed into a well. Samples were assayed using a Promega GloMax plate reader with dual injectors, using the Dual-Luciferase Reporter Assay System (Promega E1910) per manufacturer's instructions. Sixty µL of LAR II or Stop & Glo substrate were injected with a 2 s delay and a 10 s read time. Data were analyzed by calculating the Fluc/Rluc ratio for each well, then normalizing to the Fluc/Rluc ratio for siNT. Data import was carried out in Microsoft Excel, calculations were performed in JMP, and normalized data were graphed and analyzed by ANOVA followed by Holm-Šídák post-hoc testing in GraphPad Prism.

Protein isolation, SDS-PAGE analysis, and immunoblotting

MCF10A cells were seeded at 100,000 cells per well in 2 mL of media in 6-well plates and incubated at 37 °C for 24 h. Cells were transfected with a final concentration of 30 nM siRNAs or microRNA mimics in a total volume of 2250 µL as above for 72 h. Following treatment, cells were washed twice with cold 1X PBS, manually dislodged using cell scrapers (Falcon 353085), collected in 1 mL of cold 1X PBS, centrifuged at 1100 RCF for 5 minutes at 4 °C, then lysed in AZ lysis buffer (50 mM Tris pH 7.5, 250 mM NaCl, 1% Igepal, 0.1% SDS, 5 mM EDTA pH 8.0) with 1X complete protease inhibitors

(cOmplete Protease Inhibitor Cocktail, Roche 11697498001) by vortexing. Cell debris was pelleted at 21000 RCF for 15 minutes. A Bradford assay was used to determine supernatant total protein concentration. Protein aliquots were made using 5X Laemmli buffer, then boiled at 95°C for 3 minutes and loaded onto a gel or frozen at -20°C. Handcast SDS-PAGE gels (8%, 10%, 15%, or 4-18% gradient) containing 0.5% (v/v) trichloroethanol (Acros Organics 139441000) for stain-free imaging (77) were used to separate total protein at 110 V for 2 h. Total protein was imaged using the ChemiDoc stain-free imaging protocol (Bio-Rad) to ensure even loading at the gel stage. Gels were UV-activated for 5 min in the ChemiDoc. Following membrane transfer with the Trans-Blot Turbo system (Bio-Rad), blots were imaged again for total protein; these images are presented and quantified as blot loading controls. Immunoblotting was carried out using 5% (w/v) Omniblok dry milk (American Bio AB10109) in 1X PBST (1X PBS containing 5% (v/v) Tween) with primary antibodies listed below followed by 1:5000 peroxidase-linked anti-mouse or anti-rabbit IgG (Amersham NXA931 or NA934) as appropriate. Blots were developed using low- or high-sensitivity ECL reagent (Millipore WBKLS0500, Thermo Scientific 34094) for 5 minutes, then dried and imaged with the ChemiDoc. Images from the ChemiDoc were quantified using Image Lab 6.0.1 (Bio-Rad). Data were graphed and analyzed by ANOVA followed by Holm-Šídák post-hoc testing in GraphPad Prism.

Target molecule	Primary antibody manufacturer and catalog number	Dilution
FBL	Abcam ab226178	1:1000
POLR1A (RPA194)	Santa Cruz Biotechnology sc-48385 (clone C-1)	1:1000
Puromycin	Kerafast EQ0001 (clone 3RH11)	1:5000
RPS28	Invitrogen PA5-45721	1:500
SPRR3	Proteintech 11742-1-AP	1:500
TP53	Santa Cruz Biotechnology sc-126 HRP (clone DO-1)	1:5000
UBTF	Santa Cruz Biotechnology sc-13125	1:500

Puromycin incorporation for SUnSET global translation assay

After the 72 h transfection period in 2250 µL in six-well plates, MCF10A cells were treated with an additional 750 µL of media containing 3 µM puromycin (Mirus Bio 5940), achieving a final concentration of 1 µM (0.5 µg/mL) puromycin and final volume of 3 mL (46,47,55,78). Cells were incubated 1 h at 37 °C, then washed with cold 1X PBS. Protein was isolated and analyzed as above.

Identification of putative microRNA binding sites

Candidate microRNA binding sites in transcripts coding for nucleolar proteins were identified using databases including TarBase 8 (66), TargetScan 7.2 (79), and miRWalk 3 (80). Binding sites were computationally tested using the bimolecular DuplexFold algorithm on the RNAStructure Web Server (81). The sequence of either hsa-miR-28-5p or hsa-miR-708-5p was tested for *in silico* binding to 70

bp regions of target transcripts containing putative microRNA binding sites. Transcript regions bearing a scrambled binding site were also tested for binding by either mature microRNA sequence. Computed binding energies from DuplexFold are reported in this manuscript.

Molecular cloning of psiCHECK-2 plasmids for microRNA UTR assays

The psiCHECK-2 plasmid was acquired as a gift from P. Pawlica and J. A. Steitz (Yale University) (82). Transcriptomic regions of approximately 200 bp containing putative microRNA binding sites were cloned from MCF10A genomic DNA, which was isolated using the DNeasy Blood & Tissue Kit (Qiagen 69504). Primers for generating XhoI-NotI amplicons were designed using Geneious 8.1.9 (Biomatters Ltd.) (**Supplementary Table 9**). Amplicons were restriction cloned into psiCHECK-2. Target WT seed sequences were scrambled by site-directed mutagenesis overlap cloning (83). Plasmids were verified by Sanger sequencing (GENEWIZ, Inc./Azenta Life Sciences).

MicroRNA UTR assays testing for direct interaction of microRNA mimics with putative mRNA targets

MCF10A cells were seeded at 40,000 cells per well in 1 mL of media in 24-well plates and incubated at 37 °C for 24 h. Cells were co-transfected for 24 h with 30 nM siRNA or microRNA mimic, 10 ng of psiCHECK-2 plasmid, and 1 µg of salmon sperm carrier DNA using Lipofectamine 3000 (Invitrogen L3000015) according to manufacturer protocol. Following treatment, cells were washed with 1 mL of 1X PBS and incubated in 100 µL of 1X Passive Lysis Buffer (Promega E1941) at room temperature for at least 30 minutes. The dual-luciferase assay was carried out as detailed above. Data were analyzed by calculating the Rluc/Fluc ratio for each well, then normalizing to the Rluc/Fluc ratio for siNT. Data import was carried out in Microsoft Excel, calculations were performed in JMP, and normalized data were graphed and analyzed by ANOVA followed by Holm-Šídák post-hoc testing in GraphPad Prism.

miR-eCLIP analysis for identifying direct targets of MIR-28 family members

miR-eCLIP was performed as detailed in (84). Briefly, 3.5 million MCF10A cells were seeded into 15 cm tissue culture dishes and incubated for 48 h in 10 mL media. Cells were transfected with either hsa-miR-28-5p or hsa-miR-708-5p microRNA mimics at 30 nM using RNAiMAX (see above). After 27 h, cells were washed with 15 mL 1X PBS, covered with 5 mL 1X PBS, UV crosslinked with 254 nm light at 400 mJ/cm^2, and collected by scraping. Approximately 10 million crosslinked cells from each microRNA mimic treatment were pooled and processed for miR-eCLIP sequencing and data analysis (Eclipse Bioinnovations, San Diego, CA). Raw reads for the AGO2 immunoprecipitation (IP) and the

size-matched input are available at NCBI under BioProject accession PRJNA923105. Processed data are available in **Supplementary Table 10**.

Statistical testing

Statistical tests are outlined above and in the Figure Legends. Biological replicates are shown in the figures and sample sizes are noted in the Figure Legends. Statistical tests were conducted in JMP or GraphPad Prism 8. Unless otherwise stated in the Figure Legends, tests were conducted using siNT as the comparator, and *p* value magnitude is represented as *****, $p < 0.05$; ******, $p < 0.01$; *******, $p < 0.001$.

Results

A high throughput phenotypic screen for altered nucleolar number identifies 71 novel microRNAs that negatively regulate ribosome biogenesis

Following on the success of our previous nucleolar number-based screens for novel RB regulators (46,47), we hypothesized that microRNAs could also be functioning as nodes of control for RB. To discover novel microRNA negative regulators of ribosome biogenesis, we screened an arrayed library of 2603 human mature microRNA mimics (Dharmacon/Horizon Discovery) for their ability to alter nucleolar number 72 h after transfection into human MCF10A cells (**Figure 1A**). While most MCF10A cells treated with a negative control non-targeting siRNA (siNT) display between two and four nucleoli, cells depleted of the tUTP NOL11 (siNOL11) have an increased probability of having one nucleolus per nucleus (“one-nucleolus phenotype”), while those depleted of the mitotic kinesin KIF11 (siKIF11) have an increased probability of having five or more nucleoli per nucleus (“5+ nucleoli phenotype”) (**Figure 1B**, siNT, siNOL11, or siKIF11 panels). Using these siRNAs as controls, we employed our established high-throughput nucleolar number screening platform to count nucleolar number after overexpression of microRNAs by using the CellProfiler software to segment and enumerate FBL-stained nucleoli on a per-cell basis from images captured by an automated microscope.

We took several steps to ensure our screen’s reproducibility and minimize false positives. We conducted the primary screen in biological triplicate, enabling robust calculation of one-nucleolus percent effect and 5+ nucleoli percent effect for each microRNA mimic. To assist with hit selection, we also calculated the strictly standardized mean difference (SSMD) for each microRNA mimic. SSMD is a more robust estimator of hit effect size than percent effect alone, as it also incorporates information on sample size and reproducibility (variance) while simultaneously controlling the false positive and false negative rates (85). Using these two cutoffs in concert allowed us to pick the

strongest, most replicable hits. The percent effect cutoff was set at the top 2.5% for the one-nucleolus effect and at the top 1.0% for the 5+ nucleoli effect; the SSMD cutoff was set at 1.645 for both phenotypes, which allows identification of hits that are at least fairly strong (58). The median signal-to-background (S/B) for the controls was 2.74 or 2.64 for the one-nucleolus screen or the 5+ nucleoli screen, respectively. The median Z' factor for the one-nucleolus screen was 0.41, although the median Z' factor for the 5+ nucleoli screen was unfavorable at -0.43. Despite poor separation of controls for the 5+ nucleoli screen, reflected in the low median Z' factor, we felt confident that imposing a stricter percent effect cutoff and maintaining the strong SSMD cutoff would enable us to identify hits with reproducible increases in nucleolar number.

Using stringent cutoffs for mean percent effect and SSMD, the nucleolar number primary screen identified 64 one-nucleolus hits and nine 5+ nucleoli hits (**Figure 1C-D, Supplementary Tables 2-3**). The SSMD cutoff approach allowed us to ignore a number of less reproducible hits with otherwise high mean percent effect values, mostly from the 5+ nucleoli side of the screen (**Figure 1C-D**, bottom right quadrant of each graph). This total of 73 hits equates to an overall 2.8% hit rate. Inspection of images from top hits including hsa-miR-548an, hsa-miR-708-5p, and hsa-miR-629-3p (**Figure 1B**) confirmed that the relevant phenotype for each hit was observed. We performed a validation screen with replicates for the 73 hits, where each hit was picked from the original microRNA mimic library and rescreened on a new plate for a change in nucleolar number. Overall, 71/73 hits (97%) passed validation (**Supplementary Figure 1, Supplementary Table 3**).

We also screened a library containing 2609 microRNA inhibitors (Dharmacon/Horizon Discovery) in biological triplicate to investigate whether any microRNAs expressed in MCF10A cells were positively regulating RB. This screen had overall fewer actives and greater variability among replicates (**Supplementary Table 4**). Therefore, no microRNAs were consistently identified to be positively regulating RB in this screening campaign in MCF10A cells.

Novel microRNA negative regulators of ribosome biogenesis preferentially target transcripts encoding proteins in the nucleolus or involved in cell cycle regulation

We hypothesized that the microRNA mimic hits from the primary screen would be more likely to target genes whose product is nucleolar or is involved in processes affecting the nucleolus. We sought to combine bioinformatic databases containing microRNA:target RNA pairs, MCF10A RNA expression data, and catalogs of known nucleolar proteins to test this hypothesis. To investigate the hits' targets, we utilized TarBase 8, a catalog of over 670,000 experimentally-validated microRNA:target RNA interactions collected from the literature (66). We filtered TarBase 8 to only include 373,890 human microRNA:target interactions with a "down" regulatory relationship (**Figure 2A**). We assembled an MCF10A RNA expression dataset from 4 independent RNAseq experiments

(BioProject accessions PRJNA290557, PRJNA384982, PRJNA530983, PRJNA647393) to determine which RNAs were expressed in this cell line. We discovered 20,345 genes bearing one or more transcripts with a normalized (zTPM) expression value greater than -3 in at least one RNAseq experiment (**Supplementary Table 5**), supporting expression for each of these genes (59). We used our RNA expression dataset to further filter out all target genes that were not expressed in MCF10A cells from TarBase 8, after which 1,074 microRNAs and 351,983 microRNA:target interactions remained (**Figure 2A**). Furthermore, we merged three nucleolar protein databases (63-65) to create a nucleolar protein reference metadatabase containing 3,490 unique nucleolar proteins (**Figure 2A, Supplementary Table 6**). Using these three datasets, we labeled all microRNA:target interactions potentially present in MCF10A cells that contain targets encoding nucleolar proteins. Only 32/71 (45.1%) of the microRNA hits had at least one experimentally-validated target in TarBase 8 (**Figure 2A**); however, this figure is consistent with the fact that only 1,074/2,603 (41.3%) microRNAs in the primary screening library are represented in TarBase 8.

To investigate our hypothesis that hit microRNAs preferentially target transcripts encoding nucleolar proteins, we compared the 32 hit microRNAs to the remaining 1,042 non-hit microRNAs in our filtered, annotated TarBase 8 database (**Figure 2B**). We counted the number of transcripts coding nucleolar proteins that are targeted by each microRNA. We find that the median number of nucleolar targets for the hit microRNAs is 54, compared to the median value of 40 for 1,042 non-hit microRNAs, confirming enrichment and supporting our hypothesis (**Figure 2B**). We also identified 262 genes expressed in MCF10As that are targeted by at least 5 of the novel microRNA hits, representing the top 3.7% of genes most frequently targeted by the hits (**Figure 2A, Supplementary Table 7**). GO analysis of these genes revealed enrichment for encoded functions in cell cycle regulation, TP53 signaling, cellular proliferation, and for localization within the nucleolus (**Figure 2C**). Altogether, these data support the hypothesis that the novel microRNA hits preferentially target transcripts encoding proteins localized to the nucleolus or involved in cell cycle regulation.

A majority of novel microRNA negative regulators of ribosome biogenesis strongly inhibit nucleolar rRNA biogenesis

To more directly determine the extent to which the novel microRNA hits can abrogate nucleolar function, we harnessed our laboratory's high-throughput assay for nucleolar rRNA biogenesis inhibition (54). Briefly, we previously optimized and miniaturized a nascent rRNA assay using 5-ethynyl uridine (5-EU) metabolic labeling to quantify changes in nucleolar 5-EU signal by co-staining for the nucleolar protein FBL/fibrillarin (**Figure 3A**). Our assay is sensitive to defects in pre-rRNA transcription, processing, or modification, which we collectively refer to as nucleolar rRNA biogenesis (54). We established an empirical cutoff for nucleolar rRNA biogenesis inhibition of 50%, as we

discovered that depletion of almost all RB factors we tested during validation caused inhibition at or above this value (54). Furthermore, factors involved in both pre-rRNA transcription and processing typically caused the highest percent inhibition values, followed by factors only involved in pre-rRNA transcription, pre-rRNA processing, or pre-rRNA modification, respectively.

We conducted a secondary screen with five biological replicates for nucleolar rRNA biogenesis inhibition on all 71 microRNA mimics that passed primary screen validation as well as one additional microRNA mimic in the original library as a positive control, hsa-miR-34a-5p. We chose to include both hsa-miR-34a strands, as the *MIR34A* locus has been implicated in Wnt-mediated control of RB (86), and hsa-miR-34a-5p targets the *RMRP* RNA which is critical for pre-rRNA processing (87,88). Following treatment, cells were fixed and stained for FBL and 5-EU incorporation (**Figure 3B**), before image processing and quantification were completed with CellProfiler. As expected, MCF10A cells treated with siNT had robustly active nucleoli (**Figure 3B**, siNT panel), while positive control cells depleted of the RNAP1 subunit POLR1A (siPOLR1A) showed strongly decreased nucleolar rRNA biogenesis (**Figure 3B**, siPOLR1A panel) (54). Acute treatment with BMH-21, a known small molecular inhibitor of RNAP1 (89,90), at 1 μM for 1 h also eliminated nucleolar 5-EU signal as expected (54) (**Figure 3B**, siNT + BMH panel). For the secondary screen replicates (n = 5), the median Z' factor was 0.27 and the median S/B was 1.88, indicating acceptable separation of controls.

Remarkably, the secondary screen indicated that 51/72 (70.8%) microRNA mimic hits assayed caused at least a 50% inhibition of nucleolar rRNA biogenesis (**Figure 3C, Supplementary Table 3**). Notably, all eight 5+ hits tested strongly inhibited nucleolar rRNA biogenesis, with a mean percent inhibition of 92.6%. These data support the hypothesis that most microRNA hits from the primary screen significantly disrupt nucleolar rRNA biogenesis, the main function of the nucleolus.

A diverse subset of 15 microRNA hits was chosen for mechanistic follow-up

We chose a subset of 15 microRNA hits to further study for their specific effects on crucial RB subprocesses, including pre-rRNA transcription, pre-rRNA processing, and global protein synthesis. We prioritized selecting a diverse group of microRNAs that were representative of differences in key variables observed in the screening campaign, but also were considered to be authentic, valid microRNAs by sequencing and evolutionary analyses. To this end, we conducted principal component analysis to visualize screening and bioinformatic data in a dimension-reduced format (**Figure 4A-B**). A major cluster containing most one-nucleolus hits with relatively few validated nucleolar targets was apparent, accompanied by outliers that either were 5+ nucleoli hits or had a high number of validated nucleolar targets (**Figure 4A**). To minimize the potential for studying biological false positives, we also classified hits according to their evolutionary conservation, as cataloged by MirGeneDB (91), or their sequencing read quality consistency across 28,866 small

RNAseq experiments (92). The latter analysis accounted for the compliance of small RNAseq reads with Dicer processing rules, particularly the minimal variability of microRNA sequences at the 5' terminus, and for coverage across the microRNA precursor transcriptome annotation.

For further mechanistic assay validation, we combined our PCA analysis, microRNA conservation data, and manual literature curation to select 12 one-nucleolus hits, two 5+ nucleoli hits, and hsa-miR-34a-5p, which was not a hit in the primary screen but did significantly inhibit nucleolar rRNA biogenesis (**Figure 4C**). The median nucleolar rRNA biogenesis percent inhibition of these hits was 72.2% with a range of -26.3% to 130.3%. Of these hits, 10 were recorded in MirGeneDB and were classified as "High Confidence" microRNAs annotated in miRBase (92), while 5 were not in MirGeneDB and were classified as "Low Confidence" microRNAs in miRBase (**Supplementary Table 3**). Additionally, 14/15 hits passed a tripartite filter for sequencing read quality consistency (92). Two microRNA hits from the MirGeneDB MIR-28 family (91), hsa-miR-28-5p and hsa-miR-708-5p, were included in the subset.

A subset of microRNA hits dysregulates pre-rRNA transcript levels and rDNA promoter activity

Since many microRNA hits caused strong inhibition of nucleolar rRNA biogenesis in the secondary 5-EU screen, we hypothesized that these hits might dysregulate pre-rRNA transcription directly by targeting the 47S primary transcript. We tested this hypothesis by comparing the number of predicted canonical seed binding sites on the 47S pre-rRNA transcript (transcript NR_046235.3) for each of the 72 hits with its corresponding mean nucleolar rRNA biogenesis percent inhibition (**Supplementary Figure 2A; Supplementary Table 11**). Surprisingly, we did not observe a strong correlation, with several hits having a high nucleolar rRNA biogenesis percent inhibition and zero predicted 47S binding sites.

To experimentally test the 15 subset hits' effects on RNAP1 transcription, we measured the steady-state levels of the 45S pre-rRNA transcript as a proxy for transcription after treatment with the subset of microRNA mimics or control siRNAs by RT-qPCR. (**Supplementary Figure 2B**). While depletion of the transcription (t)UTP NOL11 led to a stark decrease in 45S levels versus siNT as expected (93), none of the microRNA hits statistically-significantly altered 45S levels (**Supplementary Figure 2C**). However, 4 microRNA hits (hsa-miR-34a-5p, hsa-miR-212-5p, hsa-miR-330-5p, hsa-miR-526b-5p) caused a mean decrease in 45S levels of at least 50% [less than -1 $\log_2$(45S transcript levels)]. However, considerable experimental noise with this assay may mask the true effect of these microRNA mimics on altering 45S transcript levels.

To further interrogate pre-rRNA transcription, we conducted a dual-luciferase reporter assay for RNAP1 promoter activity (55,94) after microRNA mimic expression. The assay uses a firefly

luciferase reporter under the control of the rDNA promoter and a *Renilla* luciferase reporter constitutively driven by a CMV promoter to normalize for transfection efficiency (**Supplementary Figure 2D**). Strikingly, we found that treatment with the 15 microRNA hits had diverse effects on RNAP1 promoter activity: 3 microRNA mimics (hsa-miR-147a, hsa-miR-526b, hsa-miR-548an) caused a decrease in RNAP1 promoter activity; 5 microRNA mimics (hsa-miR-34a-5p, hsa-miR-124-3p, hsa-miR-330-5p, hsa-miR-629-3p, hsa-miR-646) caused an increase in RNAP1 promoter activity; and the other 7 microRNA mimics did not cause a significant effect (**Supplementary Figure 2E**). Compared to mock and siNT negative controls, siNT treatment followed by 1 μM BMH-21 dosage significantly decreased RNAP1 promoter activity, while NOL11 depletion caused a modest but statistically-insignificant defect (**Supplementary Figure 2E**). Conversely, depletion of the cytoplasmic RP RPL4 had no effect on RNAP1 promoter activity (**Supplementary Figure 2E**). These results indicate that the microRNA hits do not reliably affect pre-rRNA transcription as measured by 5-EU incorporation or 45S transcript levels, while they may upregulate, downregulate, or have no effect on RNAP1 promoter activity. Future experiments may be required to better understand the interplay between microRNA activity and pre-rRNA transcription.

A subset of microRNA hits dysregulates maturation of the 30S pre-rRNA precursor

Given the inconclusive ability of the microRNA hit subset to consistently regulate pre-rRNA transcription, we also hypothesized that these hits could affect pre-rRNA processing, another component of nucleolar rRNA biogenesis (54). We carried out northern blotting for all 15 microRNA hits in the subset, probing for pre-rRNA processing intermediate molecules containing either ITS1 (P3 probe) or ITS2 (P4) probe (**Figure 5A**). Surprisingly, ITS1 blots broadly demonstrated that most microRNA hits dysregulated maturation of the 30S pre-rRNA precursor (**Figure 5B-C**). Ratio Analysis of Multiple Precursors calculations [RAMP, (76)] indicated 3 major clusters of pre-rRNA processing defects caused by the microRNA hits, namely, no change (n.c.), a 30S down cluster, and a 30S up/21S down cluster (**Figure 5C-D**). The last cluster contained two subclusters, one with hits causing a moderate 21S processing defect (“30S↑, 21S↓” in **Figure 5D**) and another with hsa-miR-28-5p and hsa-miR-708-5p which caused a severe 21S processing defect (“30S↑, 21S↓↓” in **Figure 5D**). We also examined the extent to which ITS2 processing was dysregulated by the subset of microRNA hits (**Supplementary Figure 3A**). We discovered that hsa-miR-708-5p and the two 5+ nucleoli hits, hsa-miR-212-5p and hsa-miR-629-3p, each caused a mild increase in 32S levels and a mild decrease in 12S levels; additionally, hsa-miR-330-5p mildly attenuated levels of the 32S and 12S precursors (**Supplementary Figure 3B-C**). The remaining microRNA hits did not cause a significant change in ITS2-containing precursor levels.

We conducted BioAnalyzer electrophoresis to define the ability of the microRNA hits to modulate steady-state levels of mature 28S and 18S rRNAs (**Figure 5A**). BioAnalyzer quantification revealed an increase in the mature 28S/18S rRNA ratios for 3 microRNA hits: hsa-miR-28-5p, hsa-miR-708-5p, and hsa-miR-4730 (**Figure 5E**), portending a defect in 18S maturation. Indeed, calculation of the ratio of mature 18S rRNA to total RNA from the electropherogram data showed stark decreases in 18S levels following treatment with any of these three microRNAs (**Figure 5E**). Methylene blue staining corroborated the increase in 28S/18S ratio for hsa-miR-28-5p and hsa-miR-708-5p (**Figure 5F**), although this technique has lower precision than BioAnalyzer quantification. All three microRNAs with deficient mature 18S rRNA levels were in the severe 21S processing defect cluster, consistent with the pre-rRNA processing pathway (**Figure 5A**), and hsa-miR-4730 clustered at the interface between the moderate and severe 30S defect subclusters (**Figure 5D**). The other 12 microRNA mimic hits did not cause a significant change in mature rRNA levels. Together these results reveal, for the first time, the dysregulatory potential of microRNAs to interfere with major steps in pre-rRNA processing.

A subset of microRNA hits decreases global translation

We also hypothesized that overexpression of the microRNA hits might repress global translation. We used the SUnSET puromycin labeling assay (78) to quantify the extent to which each microRNA hit could inhibit global protein synthesis. Following a 72 h transfection period, MCF10A cells were metabolically labeled for 1 h with 1 μM puromycin, which is incorporated into nascent peptides. Total puromycin was measured as a proxy for global translation rate by immunoblotting total protein with an α-puromycin primary antibody. Treatment with 14/15 (93.3%) of the microRNA hits significantly decreased global protein synthesis relative to the negative non-targeting siRNA control (**Figure 6A-B**). A similar decrease was observed for the positive control, an siRNA depleting the 60S subunit member RPL4 (**Figure 6A-B**). In total, these results indicate that nearly all of the subset microRNA hits inhibit global protein synthesis, the ultimate objective of ribosome biogenesis.

A subset of microRNA hits alters levels of TP53 or *CDKN1A* (*p21*)

Since treatment with many microRNA mimic hits significantly inhibited nucleolar rRNA biogenesis and normal pre-rRNA processing, we hypothesized that treatment with the hits may activate the nucleolar stress response via TP53 stabilization and *CDKN1A* (*p21*) upregulation. The nucleolar stress response is induced following disruption of RB subprocesses or the normal tripartite nucleolar structure (17,19,95). Mechanistically, 5S RNP proteins including the 60S RPs RPL5 or RPL11 can bind and sequester MDM2, the E3 ubiquitin ligase targeting TP53 for constitutive degradation. Derepression of TP53 then upregulates *CDKN1A* (*p21*) expression, which acts in

concert with TP53 to arrest the cell cycle and initiate apoptosis. We tested the first part of our hypothesis by immunoblotting for steady-state TP53 levels to assess how microRNA hit overexpression affected nucleolar stress response induction (**Figure 6C**). Six of the 15 microRNA hits stabilized TP53 levels, while surprisingly, hsa-miR-629-3p significantly decreased steady-state levels of TP53 (**Figure 6C-D**). The remaining 8/15 microRNAs did not cause significant dysregulation of TP53 levels. Depletion of either the tUTP factor NOL11 or the 60S RP RPL4 strongly stabilized TP53 as expected (**Figure 6C-D**).

We also investigated how the microRNA hits affected *CDKN1A* (p21) mRNA transcript levels by RT-qPCR. Again, depletion of the positive control NOL11 robustly increased *CDKN1A* levels as compared to siNT, while 11/15 microRNA mimics also upregulated *CDKN1A* to a statistically-significant degree (**Figure 6E**). These data largely concur, although there are two notable discrepancies. First, hsa-miR-28-5p and hsa-miR-708-5p caused strong TP53 stabilization yet did not elicit measurable *CDKN1A* upregulation, which we address in the next section. Second, hsa-miR-629-3p strongly decreased steady-state TP53 levels while simultaneously inducing *CDKN1A*. These results indicate that the hits have diverse abilities to induce the nucleolar stress response for cell cycle interruption via upregulation of TP53 or *CDKN1A*.

Two microRNA hits, hsa-miR-28-5p and hsa-miR-708-5p, are family members who each downregulate *RPS28* and the oncogene *SPRR3*

During our mechanistic studies of the 15 microRNA hits, we hypothesized that the two included MIR-28 family members, hsa-miR-28-5p and hsa-miR-708-5p, would elicit similar results from each assay because of their identical seed sequences. These two microRNAs share the same 7 nt seed sequence (AGGAGCU) (**Figure 7A**) (91). Indeed, we observed similar cellular RB phenotypes following hsa-miR-28-5p or hsa-miR-708-5p treatment, including the same aberrant pre-rRNA processing signature and stark decreases in both mature 18S rRNA levels and global protein synthesis (**Figure 7A**). To uncover potential mechanisms for these phenotypic changes, we conducted RNAseq and differential expression analysis for cells treated with hsa-miR-28-5p or hsa-miR-708-5p versus non-targeting siRNA (siNT) to control for nonspecific effects of small RNA transfection (**Figure 7B, Supplementary Table 8**). We hypothesized that differential gene expression should correlate strongly between the two microRNA siblings on a per-gene basis, given that the microRNAs should be largely sharing targets due to their identical seed sequences. Remarkably, when graphing per-gene $\log_2$ expression changes for hsa-miR-708-5p (y-axis) versus hsa-miR-28-5p (x-axis) relative to the negative control, the line of best fit was close to y = 0 + 1x with an R^2 value of 0.61 (**Figure 7B**). Such a strong correlation indicates treatment with either hsa-miR-28-5p or hsa-miR-708-5p has a very similar effect on expression across the transcriptome, with the expression of

individual genes increasing or decreasing, on average, to the same degree following treatment with either microRNA. These data strongly support the conclusion that treatment with hsa-miR-28-5p or hsa-miR-708-5p have similar phenotypic effects on MCF10A cells, and also that both microRNA hits cause highly-similar changes to the transcriptome as expected for two microRNAs with the same seed sequence.

Using our differential expression analysis, we followed up on two genes, *RPS28* and *SPRR3*, strongly co-downregulated by each MIR-28 sibling microRNA (**Figure 7B-C**). RPS28 is a ribosomal protein component of the 40S subunit, and its depletion in human cells causes the same 30S up, 21S down aberrant pre-rRNA processing signature (96,97) that we observed following treatment with hsa-miR-28-5p or hsa-miR-708-5p. SPRR3 is an oncogene in breast (98), colorectal (99,100), kidney (101), brain (102), and lung tissues (103,104) controlled by the onco-transcription factor *JUN* (104,105). Our laboratory previously identified SPRR3 as a novel candidate protein regulator of ribosome biogenesis (46), but its precise mechanism of action in RB remains undefined. We validated the miR-induced downregulation of *RPS28* or *SPRR3* by each microRNA hit at the transcriptomic and proteomic levels (**Figure 7D-E**).

Given that both hsa-miR-28-5p and hsa-miR-708-5p treatment caused such a significant decrease in levels of *RPS28* or *SPRR3*, we hypothesized that transcripts of these genes may be directly targeted by the MIR-28 family. We identified two tandem putative MIR-28 family binding sites in the *RPS28* mRNA 3' UTR (**Figure 7F**). By conducting *in silico* binding experiments using the DuplexFold algorithm on the RNAstructure server (81), we confirmed that the seed regions of both MIR-28 family members could favorably interact with the candidate binding region in *RPS28* (**Figure 7F**, WT lowest energy in table; **Supplementary Figure 4A-D**). Scrambling the sequence of both binding sites in the candidate region strongly abrogated the predicted interaction with hsa-miR-28-5p or hsa-miR-708-5p (**Figure 7F**, SCR lowest energy in table; **Supplementary Figure 4E-H**). We also identified two putative MIR-28 sites in the 5' UTR or CDS region of *SPRR3*. Favorable binding was predicted between the *SPRR3* 5' UTR site and each MIR-28 sibling (**Supplementary Figure 5A-B**). However, the *SPRR3* CDS region interactions predicted by DuplexFold showed interrupted seed binding (**Supplementary Figure 5C-D**), lowering our confidence that interactions with the CDS would be functional in reducing *SPRR3* expression.

Next, we sought to test the extent to which the MIR-28 siblings could directly target these putative binding sites by using luciferase 3' UTR reporter assays (82,106). Treatment with hsa-miR-28-5p or hsa-miR-708-5p inhibited reporter activity when the reporter contained the *RPS28* candidate region with WT putative binding sites (**Figure 7G**). Crucially, reporter assays carried out using the *RPS28* candidate region with scrambled putative binding sites completely rescued the microRNA-induced reporter downregulation (**Figure 7G**), supporting the conclusion that each MIR-28 family

microRNA hit directly targets the *RPS28* 3' UTR. In contrast, our reporter for the *SPRR3* 5' UTR did not show the MIR-28 mimics could directly bind to this region of *SPRR3* (**Supplementary Figure 5E**).

To search for other possible direct targets of the MIR-28 family, we pooled 10 million MCF10A cells each treated separately with either hsa-miR-28-5p or hsa-miR-708-5p mimics for 27 h to permit RISC loading and targeting, then conducted miR-eCLIP analysis for microRNA:mRNA target chimeras (84). Briefly, treated cells were UV crosslinked, pooled, and an AGO2 immunoprecipitation was performed to isolate microRNAs actively complexed to their targets. Despite limit of detection challenges from modest AGO2 enrichment, sequencing revealed 9,243 high-confidence reads consisting of microRNA:mRNA chimeras, representing functional target pairs (**Supplementary Table 10**). We uncovered 31 genes in our MIR-28 mimic RNAseq dataset bearing transcripts targeted by both MIR-28 siblings (**Supplementary Figure 6A**), including *MYC* and *CDKN1A* (*p21*) (**Supplementary Figure 7A-D**). An additional 113 genes in our MIR-28 mimic RNAseq dataset were targeted by either MIR-28 sibling (**Supplementary Figure 6B**). MIR-28 family members therefore likely directly reduce *MYC* levels, providing another avenue of RB attenuation since MYC is an RNAP1 transcription factor (107). Targeting of *MYC* by the MIR-28 family has not previously been demonstrated in TarBase 8 (66). Furthermore, *CDKN1A* was directly targeted by the MIR-28 family, providing a logical explanation for the lack of change of *CDKN1A* mRNA levels in the face of TP53 upregulation that we observed (**Figure 6D-E**, hsa-miR-28-5p or hsa-miR-708-5p). *RPS28* or *SPRR3* were not observed to be direct targets of hsa-miR-28-5p or hsa-miR-708-5p by miR-eCLIP; however, these negative results do not preclude the possibility that functional binding could occur between the MIR-28 family and *SPRR3* transcripts, especially given the likelihood that the experimental results were incomplete due to subpar detection limits. Together, these results provide strong evidence for the ability of the MIR-28 family to perturb the transcriptome identically, and to engage in direct post-transcriptional downregulation of the central RB regulator *MYC* and *RPS28*, an RP critical for normal 18S maturation.

SPRR3 is a novel positive regulator of RNAP1 transcription

Since our previous high-throughput screen identified SPRR3 as a putative novel regulator of RB (46), we first verified that SPRR3 depletion causes a change in nucleolar number. Indeed, treatment of MCF10A cells with a pool of four ON-TARGET siRNAs targeting *SPRR3* led to a significant decrease in nucleolar number relative to the siNT negative control, as was observed for positive controls siNOL11 and siRPS28 (**Figure 8 A-B**). siRNA deconvolution revealed 3/4 individual *SPRR3* siRNAs in the pool also caused a significant decrease in nucleolar number (**Supplementary Table 12**), strongly arguing against siRNA-induced off-target effects.

We hypothesized that SPRR3 depletion could inhibit RB subprocesses including nucleolar rRNA biogenesis, pre-rRNA transcription and processing, and global translation. We again utilized our 5-EU incorporation assay to test the extent to which RPS28 or SPRR3 depletion inhibits nucleolar rRNA biogenesis. Strikingly, depletion of either gene produced nucleolar rRNA biogenesis percent inhibition values above the positive control, siPOLR1A, set at 100% (**Figure 8A, C**). These results are consistent with the known role of RPS28 in ribosome assembly (96,97), and further implicate SPRR3 as a novel regulator of RB.

For further RB assays, we utilized the original pool of four siGENOME siRNAs targeting *RPS28*. We also created a custom equimolar subpool of the two most potent individual *SPRR3* siRNAs (Horizon Discovery catalog J-019976-09 and J-019976-10). We verified that treatment with siRPS28 or the custom siSPRR3 subpool significantly reduced mRNA and protein levels of each gene, respectively (**Supplementary Figure 8A-D**).

We used 45S qPCR and the dual luciferase RNAP1 promoter activity reporter assay to determine how SPRR3 depletion altered RNAP1 transcription. Treatment with siSPRR3 significantly reduced 45S transcript levels by qPCR relative to siNT negative control (**Figure 8D**). siNOL11 transfection or 1 μM BMH-21 treatment following siNT transfection also decreased 45S levels, while siRPS28 transfection did not, as expected (**Figure 8D**). SPRR3 depletion also significantly abrogated RNAP1 promoter activity relative to mock or siNT transfection (**Figure 8E**). Again, treatment with siNOL11 or co-treatment with siNT and BMH-21 decreased RNAP1 promoter activity, while depletion of the cytosolic pre-60S maturation factor SBDS did not alter promoter activity levels (**Figure 8E**). Interestingly, depletion of RPS28 reduced RNAP1 promoter activity via this assay, although this did not appear to transmit functionally as 45S levels were not consequently reduced by siRPS28 (**Figure 8D-E**). Our observations that SPRR3 depletion strongly decreases nucleolar rRNA biogenesis, 45S transcript levels, and RNAP1 promoter activity support the conclusion that SPRR3 is a novel positive regulator of RNAP1 transcription.

We probed how depletion of RPS28 or SPRR3 could alter pre-rRNA processing patterns. While RPS28 depletion did not attenuate 45S transcript levels, it did cause very stark inhibition of nucleolar rRNA biogenesis, and has been previously shown to cause a 30S up, 21S down phenotype (96). We therefore hypothesized that the high nucleolar rRNA biogenesis inhibition observed after SPRR3 depletion could be caused not only by downregulation of pre-rRNA transcription but also by interruption of the pre-rRNA processing pathway. Northern blots confirmed that RPS28 depletion resulted in 30S stabilization and 21S destabilization, but pre-rRNA processing defects were not observed after siSPRR3 treatment (**Figure 8F-G**). Instead, SPRR3 depletion resulted in northern blots where all precursors are decreased, similar what is observed upon NOL11 depletion (**Figure 5B-C**), consistent with inhibition of pre-rRNA transcription (93). Additionally, we quantified the

28S/18S mature rRNA ratio and 18S/total RNA ratio following RPS28 or SPRR3 depletion, finding that siRPS28 resulted in an increase in 28S/18S ratio caused by lower 18S levels while siSPRR3 did not alter ratios of mature rRNAs (**Figure 8H**). These results bolster the conclusion that SPRR3's primary novel role in RB control is to positively regulate pre-rRNA transcription.

We conducted puromycin incorporation experiments following depletion of RPS28 or SPRR3 to test the hypothesis that each of these factors is critical for maintaining normal global protein synthesis. Indeed, siRPS28 or siSPRR3 treatment significantly diminished puromycin incorporation versus the mock or siNT negative controls, at a magnitude similar to that observed following RPL4 depletion (**Figure 8I**). Altogether, our experiments are consistent with a model in which SPRR3 is crucial for supporting pre-rRNA transcription, and thereby the intracellular supply of ribosomes and the process of cytoplasmic protein translation.

Discussion

Our work represents the first systematic foray into uncovering the complex roles of microRNAs as governors of ribosome biogenesis. Using our unbiased high-content screening platform for changes in nucleolar number, we have uncovered 72 novel microRNA negative regulators of RB. Strikingly, 51/72 hits strongly inhibited nucleolar rRNA biogenesis as measured by nucleolar 5-EU incorporation, supporting a role for the hits in antagonizing RB. Stringent selection and mechanistic validation of a subset of 15 novel microRNA hits unexpectedly revealed a major effect of hit overexpression to be dysregulation of 30S pre-rRNA processing; significantly, no specific microRNAs have yet been observed to directly affect pre-rRNA processing (35). While hits in the subset did not appear to reliably alter RNAP1 transcription, almost all subset hits inhibited global protein synthesis and caused upregulation of *CDKN1A* (*p21*), with nearly half increasing TP53 steady-state levels. We hypothesized that the microRNA hits were acting by binding to mRNAs required for nucleolar function and reducing their translatability. Bioinformatics of all the microRNA hits revealed that they were enriched for mRNA targets encoding proteins localized within the nucleolus or bearing functions in cell cycle progression, proliferation, or TP53 signaling, supporting our mechanistic hypothesis.

To further probe the hypothesis that microRNA mimic hits preferentially target nucleolar proteins, we focused on two MIR-28 family members, hsa-miR-28-5p and hsa-miR-708-5p. We chose them because they share the same 7 nt AGGAGCU seed sequence, and their overexpression causes the same RB defects, including a severe pre-18S rRNA processing defect. Comparison of RNAseq results following overexpression of either mimic resulted in identical transcriptomic profiles and

revealed *RPS28* as a putative direct target. Indeed, we found these MIR-28 family members directly target the *RPS28* 3' UTR, providing a mechanistic explanation for the observed processing defect (96,97) and supporting our hypothesis.

Transcriptomics also revealed SPRR3, a protein not previously known to regulate RB, as a candidate target of the MIR-28 family. Excitingly, we discovered that SPRR3 is essential for RNAP1 transcription. While we first identified SPRR3 as a candidate RB regulator in our genome-wide siRNA screen (46), our present work further defines its importance in facilitating RNAP1 promoter activity and normal accumulation of the 45S pre-rRNA precursor, as well as in enabling global translation. However, whether the MIR-28 siblings bind directly to *SPRR3* remains to be decisively determined. Consistent with a role in RNAP1 transcription, a recent report illustrated that SPRR3 is a positive regulator of pan-AKT phosphorylation (101), in turn likely driving RB as a key effector of the PI3K/AKT/mTOR axis that drives growth and proliferation. Pertinently, mTORC1 can activate UBTF (UBF) and RRN3 (TIF-1A) to enhance RNAP1 initiation, and can deactivate the RNAP3 inhibitor MAF1 to derepress synthesis of the 5S rRNA and tRNAs (107). We propose a model in which SPRR3 acts as a key pro-RB signal far upstream of direct rDNA regulation, consistent with its reported cytoplasmic localization (105). This novel role agrees with SPRR3's known oncogenic function (75,98-103). Our results elucidate the regulatory power held by a small oncogenic, cytoplasmic protein over the cellular nexus of translation in the nucleolus, underscoring the importance of non-nucleolar regulation of RB.

While our results point to the novel microRNA hits canonically acting to inhibit RB by post-transcriptionally downregulating target genes with nucleolar localization or functions in the cell cycle, we cannot exclude the possibility that these microRNAs may also have a more immediate role inside the nucleolus itself. A number of studies have defined nucleolar subsets of microRNAs in mammalian cells (38-40,108,109), though the function of nucleolar microRNAs remains poorly understood. It has been suggested that the nucleolus may serve as a staging platform for microRNAs to complex with target mRNAs outside the competitive, mRNA-rich cytoplasm (109), or perhaps that efflux of microRNAs from the nucleolus may be part of a stress response to the invasion of foreign genetic material (40). Additionally, AGO2 has been observed to bind to regions of rDNA possibly via rRNA-mediated tethering (37), though more research is needed to fully understand the potential of microRNAs to directly downregulate the 45S transcript. Previous studies (38,40) have observed the nucleolus to contain a number of our hits' families, including miR-19b, miR-25, miR-34a, miR-182, miR-183, miR-192, miR-330, and miR-629. However, in most cases, the microRNA strand was not indicated. Future investigation of nucleolar microRNAs may shed additional light on the potential direct impacts of the hits inside the nucleolus beyond the present scope.

Others have criticized the use of microRNA mimics (110), finding that they could perturb endogenous microRNA action (111). Our work did harness overexpression of microRNA mimics in tissue culture cells, which may have supraphysiological or gain-of-function effects relative to the normal human. Importantly, our hits did not overlap with hits of other microRNA mimic screens for cardiac regeneration (50) or G1-S transition and proliferation regulators (48), arguing against nonspecific dysregulatory effects on the transcriptome induced by pollution of cellular microRNAs by mimic overexpression. Furthermore, our 2.8% hit rate is on par with other screens, and we conducted thorough validation of a subset of 15 hits that lead to a wide range of RB-altered phenotypes. Tissue-specific differences may also have a confounding effect on hit observability of microRNA mimics or inhibitors, as microRNAs are often tuned for cell type specificity (112). While we acknowledge these technological shortcomings, we argue that systematic exploration of the role of this large set of human microRNAs has illuminated new regulatory roles for microRNAs in RB.

Based on the promiscuous nature of microRNA activity, screens with microRNA mimics have an increased scale and complexity of direct regulatory perturbation compared to previous RB screening campaigns (46,47,113-115). While prior screens used siRNA technology to surgically deplete expression of a single gene, the transfection of a microRNA mimic may directly deplete tens to thousands of mRNAs. Simultaneous manipulation of multiple gene regulatory networks with microRNAs may lead to complex, potentially-discordant cellular phenotypes. This is because assay results report an integration of many more heterogeneous expression changes than in simpler single-gene siRNA experiments. One key example from this work is that the MIR-28 siblings elevate TP53 protein levels without a concomitant increase in TP53's downstream target, *CDKN1A* (*p21*), as expected (116). Our miR-eCLIP data indicated that both MIR-28 microRNAs in fact directly target *CDKN1A in vivo*, as previously shown for hsa-miR-28-5p (117), resolving this discrepancy. While we found a straightforward explanation for this case, other discrepancies in our data likely remain. These results invite additional probing to improve our understanding of the complex functional perturbations associated with each microRNA hit.

Looking forward, we highlight our discovery of novel microRNA negative regulators of RB in the context of cancer. Differential regulation of many of the 72 hits has been observed in various tumors (87,118-151), with hits including hsa-miR-28-5p and hsa-miR-708-5p (152-161) often acting as tumor suppressors. We emphasize the enrichment of the hits' targets for involvement in the cell cycle, which is tightly intertwined with RB, nucleolar formation, and tumorigenesis (25,47,162). Additionally, microRNA mimic therapeutics are a promising avenue in oncology (163), though roadblocks including delivery and dosage have impeded achieving success in the clinic (164). Combining mimics and small molecules may enable inhibition of multiple targets or decrease required microRNA dose (164), as seen in clinical trials for hepatitis C (165,166). Given that cancer cells often

hyperactivate ribosome production (24), our study underscores the potential of harnessing conserved microRNAs for chemotherapy as standalone therapeutics or in concert with other potent small molecule inhibitors of RB like BMH-21 to simultaneously target pre-rRNA transcription and processing.

Acknowledgements and Funding Sources

We thank the members of the laboratory of S.J.B. and S. Carter for insightful information, questions, and comments throughout the manuscript writing process. We thank P. Pawlica and J. Steitz for advice on the microRNA 3' UTR luciferase assays and for sharing the psiCHECK2 plasmid (82). We thank the Yale Center for Genome Analysis (YCGA) for performing Agilent Bioanalyzer analysis, RNAseq library preparation and sequencing. We acknowledge the use of CellProfiler for image analysis [(56), http://www.cellprofiler.org/]. This work was supported by the following grants from the National Institutes of Health (NIH): 1R35GM131687 (to S.J.B.), 1F31DE030332 (to M.A.M.), and T32GM007223 (to C.J.B., M.A.M., and S.J.B.).

Figure 1

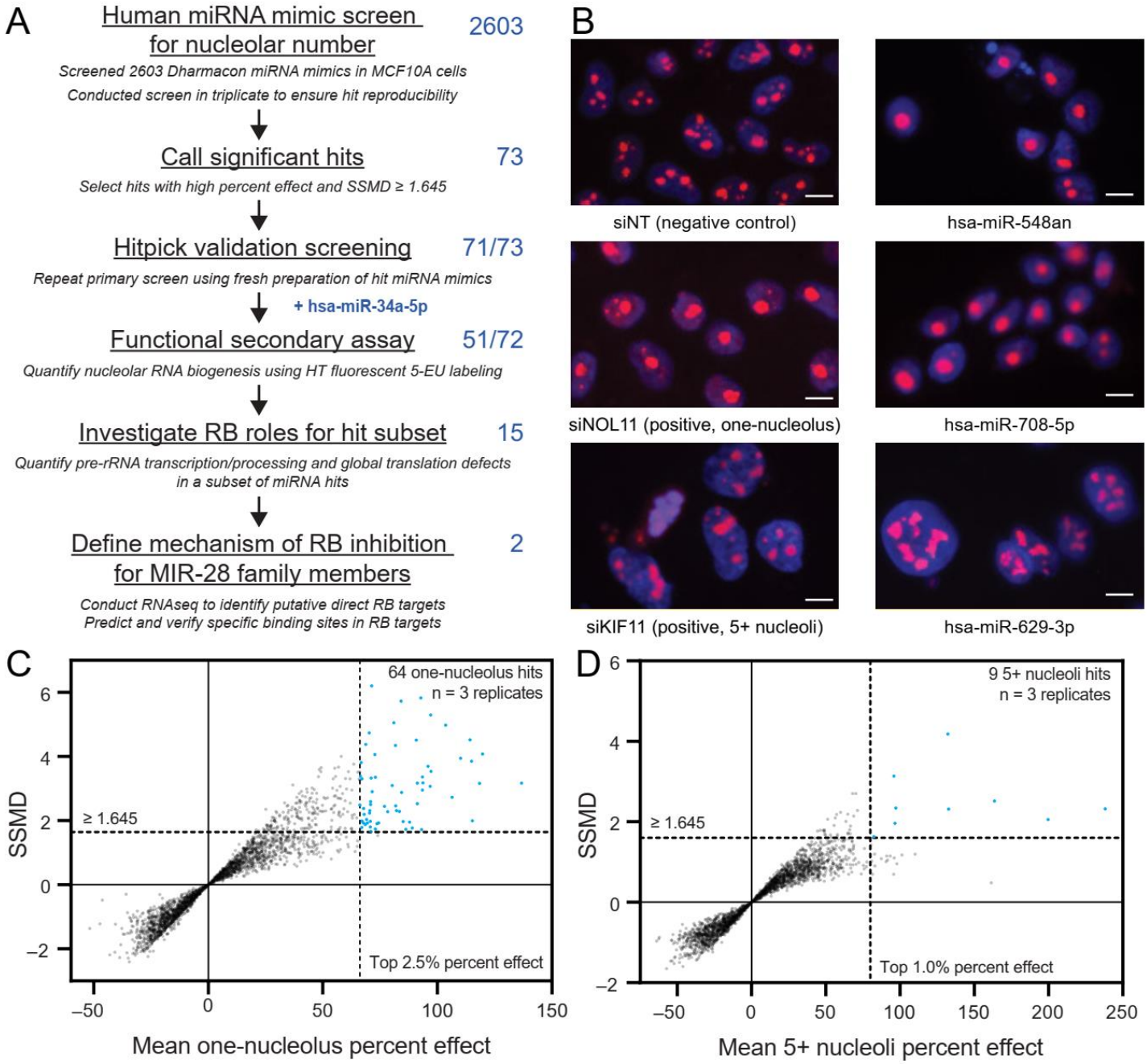

Figure 1. A screen for changes in nucleolar number reveals 71 novel microRNA mimic negative regulators of RB.

(**A**) Screening campaign pipeline. MCF10A cells were reverse-transfected into a library of 2,603 mature human microRNA mimics, then fixed and stained for DNA and FBL after 72 h in biological triplicate. The number of nucleoli was calculated using CellProfiler. Hits were called based on a decrease or increase in nucleolar number, respectively termed the one-nucleolus or 5+ nucleoli phenotypes. The primary screen identified 73 high-confidence hits, 71 of which passed hitpick validation screening. While not a primary screen hit, hsa-miR-34a-5p was included for further validation as described in the text. A functional secondary screen found that 51/73 hits strongly inhibited nucleolar rRNA biogenesis via 5-EU incorporation. Additional mechanistic assays for pre-rRNA transcription or processing, global translation, and nucleolar stress were carried out for a

subset of 15 rigorously-selected hits. Further mechanistic studies were performed on two MIR-28 family siblings, hsa-miR-28-5p and hsa-miR-708-5p.

(**B**) Representative images from the screen showing 3 top hits alongside the negative control (non-targeting, siNT) and positive controls for the one-nucleolus (siNOL11) or 5+ nucleoli (siKIF11) phenotypes. hsa-miR-548-an and hsa-miR-708-5p are hits with the one-nucleolus phenotype while hsa-miR-629-3p is a hit with the 5+ nucleoli phenotype. The DNA stain (Hoechst) is shown in blue and fibrillarin (FBL) antibody detection is shown in red. Scale bars, 10 μm.

(**C**) Double flashlight plot for one-nucleolus hit selection. A total of 64 one-nucleolus hits were called using cutoffs for the top 2.5% of mean one-nucleolus percent effect and at least fairly strong hits where SSMD ≥ 1.645 as described in the text. Data were graphed in GraphPad Prism 8.

(**D**) Double flashlight plot for 5+ nucleoli hit selection. A total of nine 5+ nucleoli hits were called using cutoffs for the top 1.0% of mean 5+ nucleoli percent effect and the same SSMD cutoff as above. Hits are shown in blue. Data were graphed in GraphPad Prism 8.

Figure 2

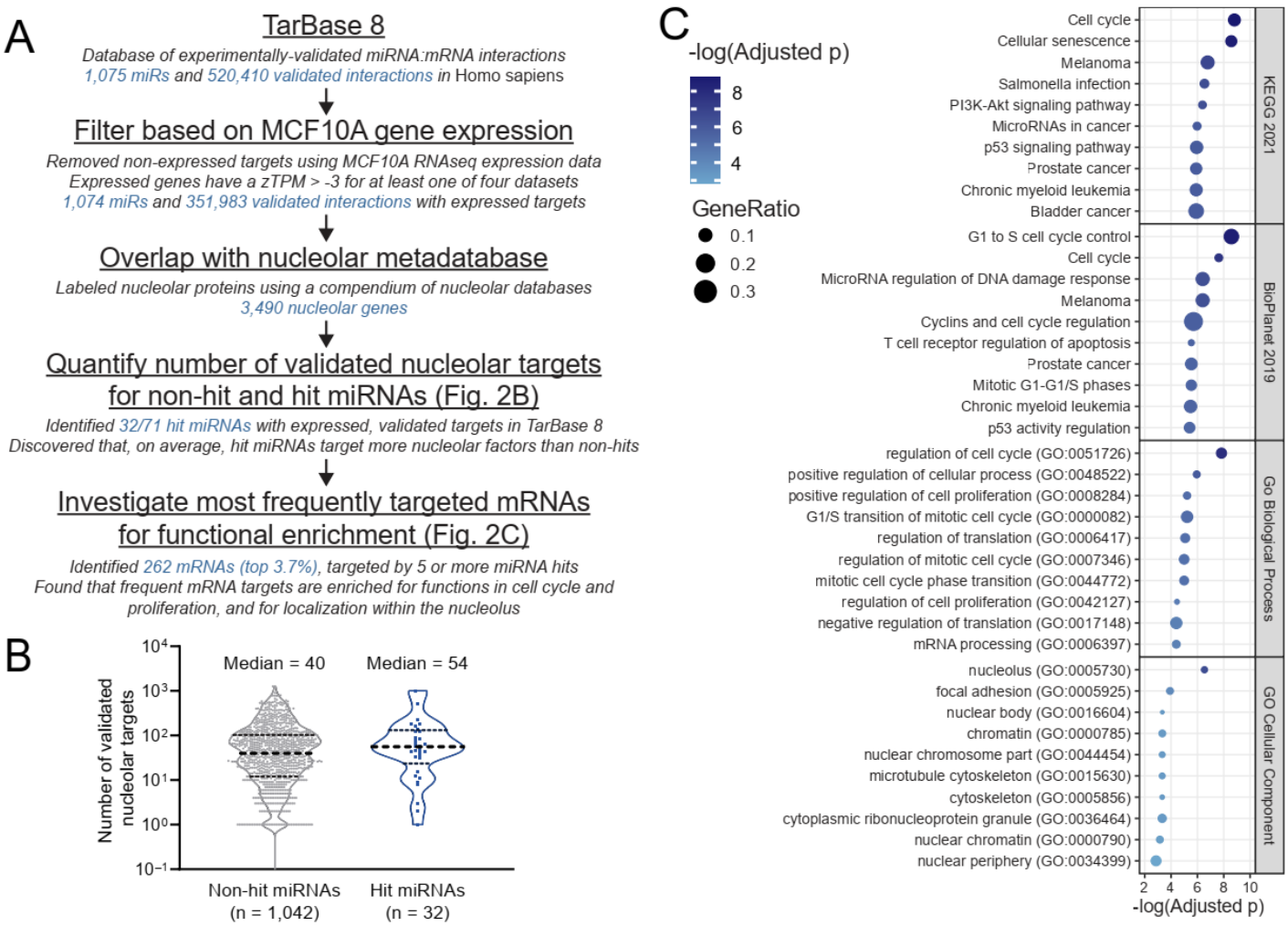

Figure 2. The novel microRNA hits preferentially target genes encoding proteins with nucleolar localization or with functions in cell cycle control.

(**A**) Bioinformatics workflow. TarBase 8 contained 520,410 validated microRNA:RNA target interactions across 1,075 mature human microRNAs. TarBase 8 was filtered for genes expressed in MCF10A cells, using a cutoff of more than -3 zTPM (normalized TPM), leaving 351,983 validated interactions. Targets were labeled for nucleolar localization based on our nucleolar proteome metadatabase containing 3,490 nucleolar proteins. MicroRNAs were grouped based on primary screen hit status, with 32/71 primary screen hits having one or more validated, expressed targets in MCF10A cells. The number of validated, expressed, nucleolar targets was calculated for hit and non-hit microRNAs. Conversely, the number of hit microRNAs targeting each gene was calculated, and all genes targeted by 5 or more hits (262, top 3.7%) were analyzed for enrichment.

(**B**) Log_{10}-scale plot indicating the number of validated nucleolar targets expressed in MCF10A cells for hit and non-hit microRNAs in TarBase 8. The median number of nucleolar targets per hit microRNA is 54, which is greater than the non-hit median of 40.

(**C**). Enrichment plots for 262 genes targeted by 5 or more of the microRNA hits. Plots indicate $-log_{10}$(adjusted *p*) on the x-axis and marker color, and the gene ratio as the marker size. Enrichment analysis was conducted with Enrichr, and plots were made in R. Enrichment databases: Kyoto

Encyclopedia of Genes and Genomes (KEGG) 2021; NCATS BioPlanet of Pathways 2019; Gene Ontology (GO) Biological Process 2018; GO Cellular Component 2018.

Figure 3

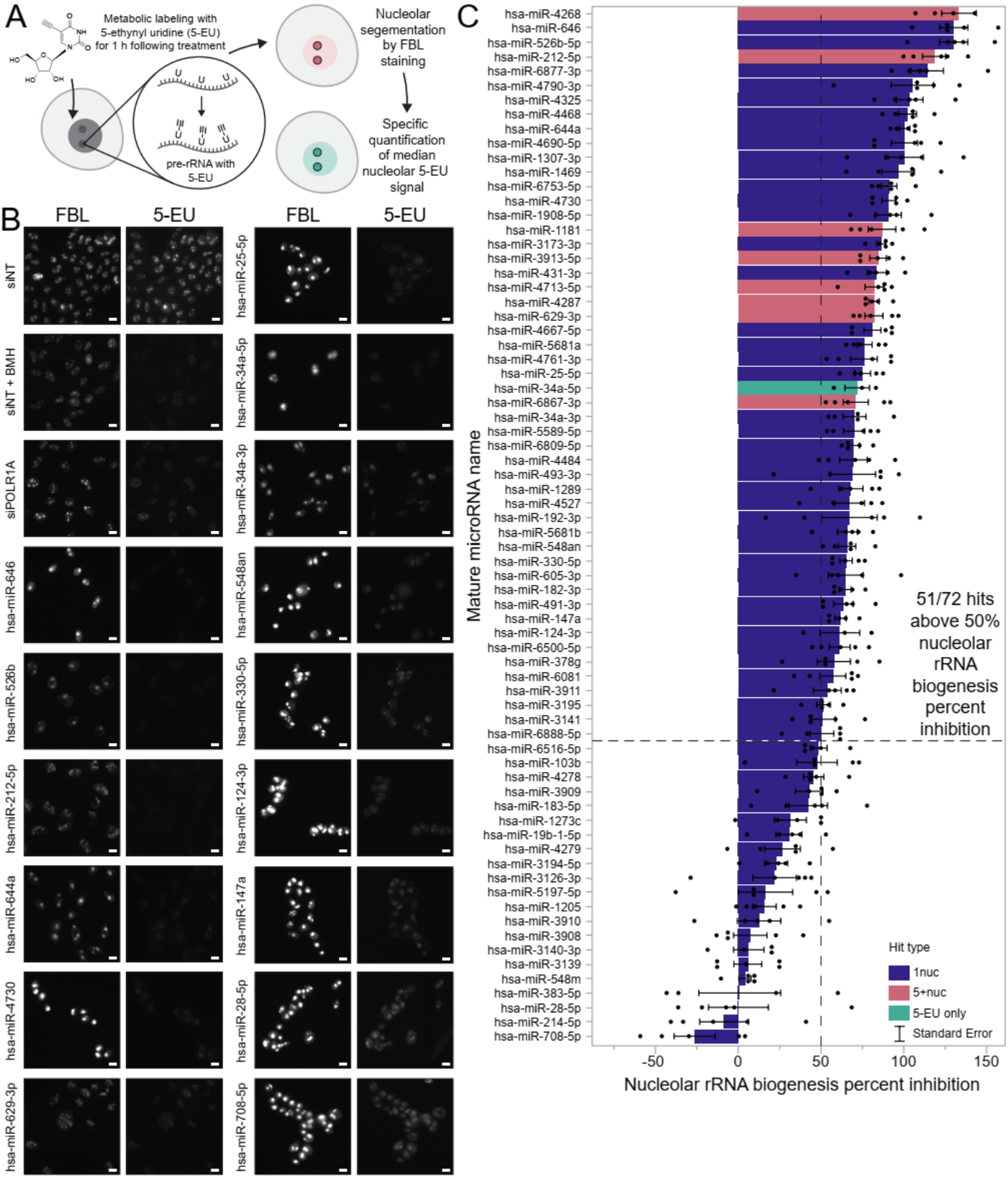

Figure 3. A secondary screen reveals 51/72 hits strongly inhibit nucleolar rRNA biogenesis.

(**A**). Schematic for the nucleolar rRNA biogenesis inhibition assay (54). Following 72 h of RNAi transfection, MCF10A cells were labeled for 1 h with 1 mM 5-ethynyl uridine (5-EU). Cells were fixed and immunostained for the nucleolar protein FBL and for 5-EU, then imaged. CellProfiler was used to segment nucleoli and calculate the median 5-EU intensity for all nucleoli per well, enabling calculation of the nucleolar rRNA biogenesis percent inhibition.

(**B**) Representative images of control- and hit-treated MCF10A cells following 5-EU incorporation. FBL immunostaining and 5-EU click labeling are shown as separate channels. Scale bars, 10 μm. siNT is the non-targeting negative control siRNA. siNT + BMH is siNT-transfected cells treated with 1 μM BMH-21 for 1 h before and during 5-EU incorporation. siPOLR1A is the POLR1A (RPA194) knockdown positive control.

(**C**). Nucleolar rRNA biogenesis percent inhibition values for 72 microRNA mimic hits. A total of 51/72 hits caused at least 50% inhibition of nucleolar rRNA biogenesis, surpassing the assay's empirical cutoff (54). siNT negative control is set to 0% inhibition, and siPOLR1A positive control is set to 100% inhibition. Hits are colored according to their primary screen phenotype; hsa-miR-34a-5p was not a primary screen hit but was included as described in the text. Mean ± SEM are shown alongside individual data points. Data were graphed in JMP.

Figure 4

A

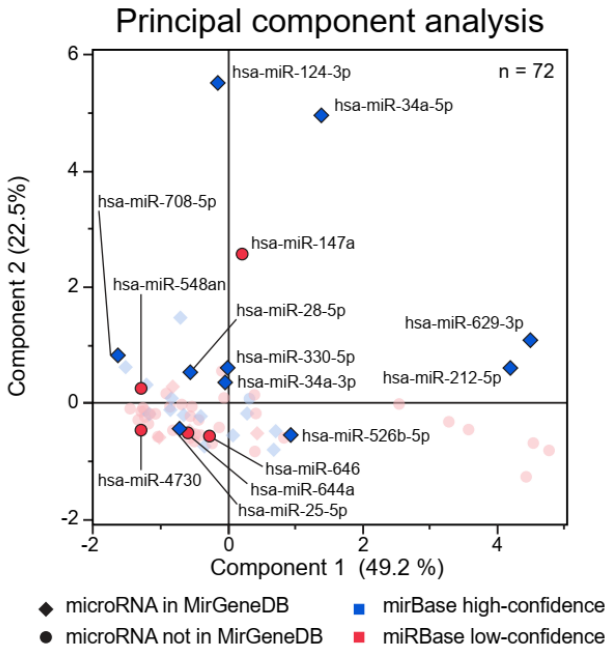

B

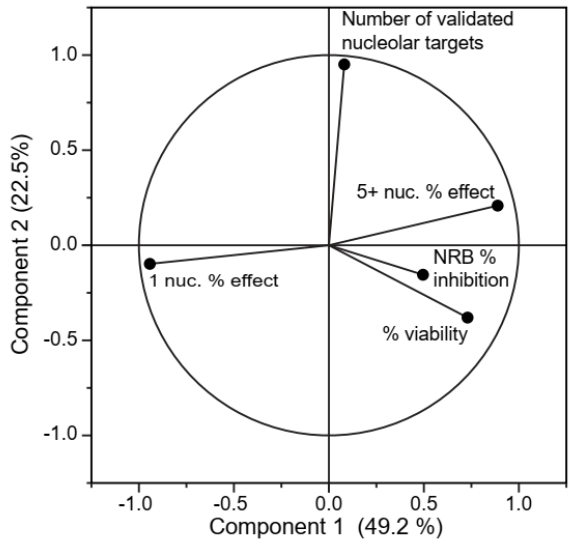

C

Mature microRNA name	miRBase accession
hsa-miR-25-5p	MIMAT0004498
hsa-miR-28-5p	MIMAT0000085
hsa-miR-34a-5p	MIMAT0004557
hsa-miR-34a-3p	MIMAT0000255
hsa-miR-124-3p	MIMAT0000422
hsa-miR-147a	MIMAT0000251
hsa-miR-212-5p	MIMAT0022695
hsa-miR-330-5p	MIMAT0004693
hsa-miR-526b-5p	MIMAT0002835
hsa-miR-548an	MIMAT0019079
hsa-miR-629-3p	MIMAT0003298
hsa-miR-644a	MIMAT0003314
hsa-miR-646	MIMAT0003316
hsa-miR-708-5p	MIMAT0004926
hsa-miR-4730	MIMAT0019852

Figure 4. A subset of 15 microRNA hits were rigorously selected for additional mechanistic validation.

(**A**) Principal component analysis (PCA) of 72 hits. The 15 selected subset hits are indicated with their mature microRNA name and are highlighted on the plot. Membership in MirGeneDB (91) or classification as high-confidence or low-confidence miRBase (92) is labeled with each hit's marker shape or color, respectively. Five variables were used for PCA including one-nucleolus and 5+ nucleoli percent effect, percent viability, nucleolar rRNA biogenesis (NRB) percent inhibition, and number of validated nucleolar targets for each hit in TarBase 8. Percentages in axis labels denote the proportion of variance explained by each PCA Component.

(**B**) Loading plot describing contribution of 5 quantitative variables to PCA Components 1 and 2 from above. Percentages in axis labels denote the proportion of variance explained by each PCA Component.

(**C**) Table of 15 mature microRNA hits selected for further validation.

Figure 5

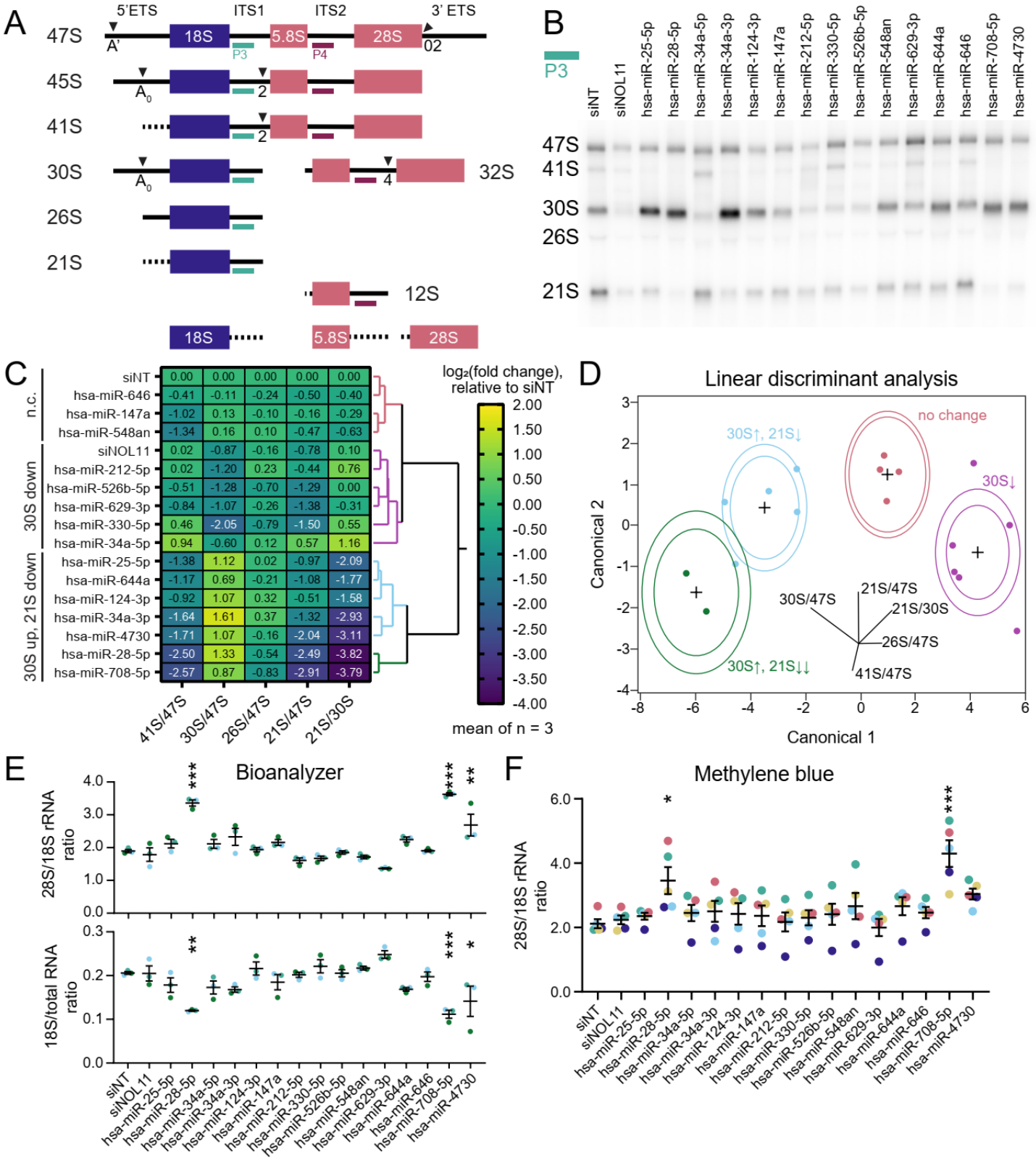

Figure 5. Most subset microRNA hits dysregulate pre-18S pre-rRNA processing.

(**A**) Simplified diagram of human pre-rRNA processing intermediates. Mature 18S, 5.8S, and 28S rRNA regions are shown as blue (pre-40S) or red (pre-60S) rectangles. Intermediate names are indicated on the left, and transcribed spacers (solid black lines) are labeled at the top. Cleavage sites are labeled with their name and represented with triangles. Dotted lines signify transcribed spacer regions digested by exonucleases. Northern blot probes P3 (teal, ITS1) or P4 (dark red, ITS2) are shown at each pre-rRNA intermediate that they bind.

(**B**) Representative ITS1 (probe P3) northern blot of 3 µg of total RNA isolated from control- or hit-treated (as indicated) MCF10A cells. Pre-rRNA processing intermediates are labeled on the left. Images were quantified using Bio-Rad Image Lab. siNT is the non-targeting negative control and siNOL11 is the positive control.

(**C**) Clustered heatmap showing $\log_2$-transformed Ratio Analysis of Multiple Precursor [RAMP (76)] calculations for microRNA hits, normalized to siNT negative control. Values represent mean $\log_2$-scale RAMP ratio for $n = 3$. Clusters: no change (n.c., red); 30S down (magenta); 30S up, 21S down (mild defect, blue and severe defect, green). RAMP ratios were calculated in Microsoft Excel. Four clusters were assigned using hierarchical Ward clustering in JMP, and data were graphed in GraphPad Prism 8.

(**D**) Linear discriminant analysis (LDA) of four 30S pre-rRNA processing defect clusters from (**C**) above. Cluster colors are the same as in (**C**). Canonical component biplot rays are shown in the graph. Ellipses represent 50% (outer) and 95% (inner) confidence levels. Data were graphed in JMP.

(**E**) Bioanalyzer analysis for 1 µg of total RNA isolated from control- or hit-treated MCF10A cells. Top, the 28S/18S mature rRNA ratio; bottom, 18S mature rRNA/total RNA ratio. Mean ± SEM are shown alongside individual data points, colored by replicate. Data were graphed and analyzed by ordinary one-way ANOVA with multiple comparisons against siNT (non-targeting negative control) and Holm-Šídák correction in GraphPad Prism 8. *****, $p < 0.05$; ******, $p < 0.01$; *******, $p < 0.001$.

(**F**) Methylene blue (MB) analysis of the 28S/18S mature rRNA ratio. Northern blots from (**B-C**) were stained with MB, imaged, and quantified using Bio-Rad Image Lab. Mean ± SEM are shown alongside individual data points, colored by replicate. Data were graphed and analyzed by ordinary one-way ANOVA with multiple comparisons against siNT (non-targeting negative control) and Holm-Šídák correction in GraphPad Prism 8. *****, $p < 0.05$; ******, $p < 0.01$; *******, $p < 0.001$.

Figure 6

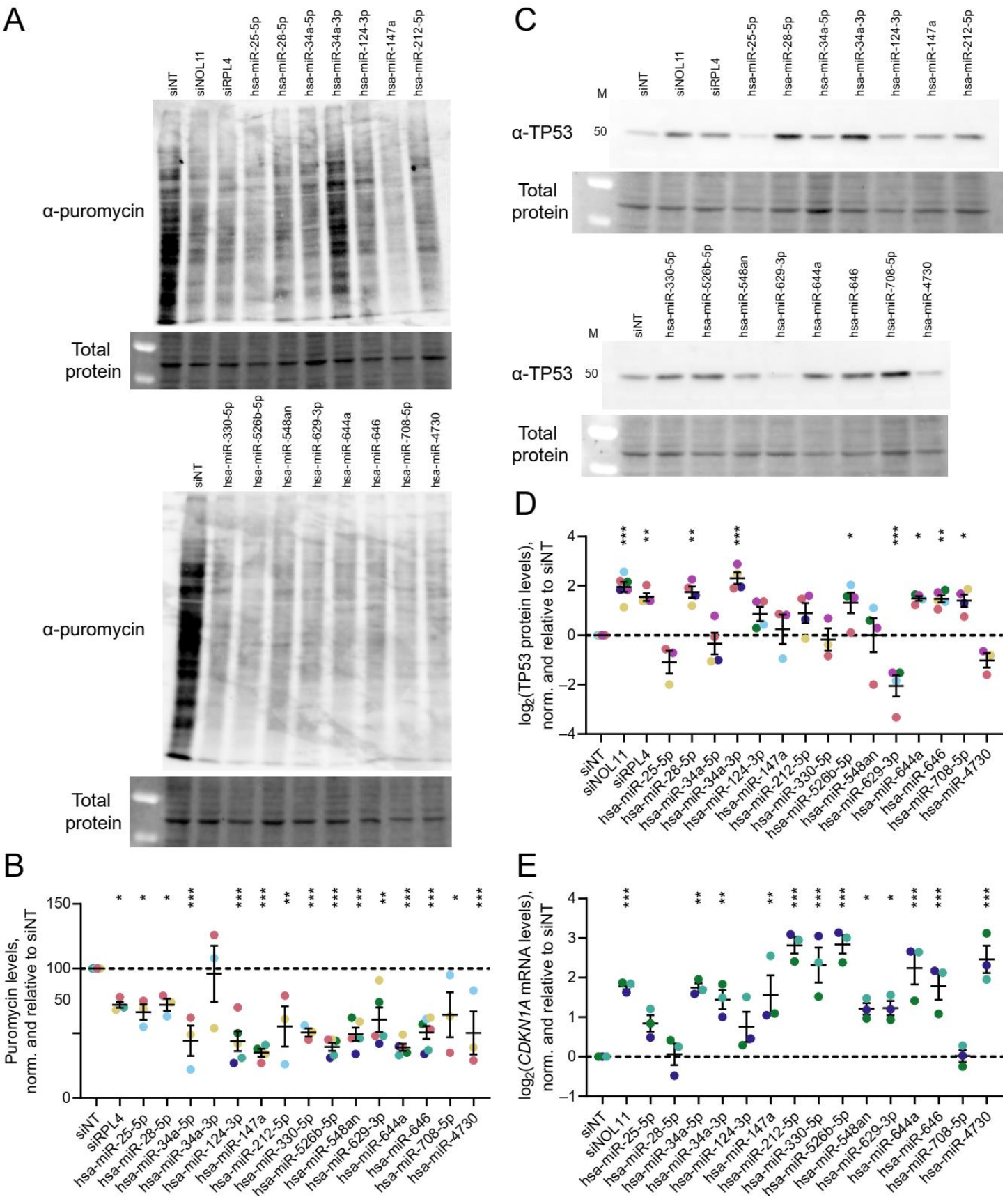

Figure 6. MicroRNA hits inhibit global protein synthesis and dysregulate levels of the cell cycle regulators TP53 and *CDKN1A*.

(**A**). Representative examples of the SUnSET puromycin incorporation assay (46,78) immunoblots of total protein isolated from control- or hit-treated MCF10A cells. α-puromycin is an immunoblot for puromycin incorporation as a proxy for global protein synthesis. Total protein is the trichloroethanol total protein stain loading control. The images were quantified with Bio-Rad Image Lab.

(**B**). Quantification of global protein synthesis levels from (**A**) above. Mean ± SEM are shown alongside individual data points, colored by replicate (at least 3 replicates per condition, with all replicates shown in the graph). The data were normalized to siNT, then graphed and analyzed by ordinary one-way ANOVA with multiple comparisons against siNT and Holm-Šídák correction in GraphPad Prism 8. *****, $p < 0.05$; ******, $p < 0.01$; *******, $p < 0.001$.

(**C**). Representative examples of TP53 immunoblots of total protein isolated from control- or hit-treated MCF10A cells. α-TP53 is the blot for TP53. Total protein is the trichloroethanol total protein stain loading control.

(**D**). Log_2-scale quantification of TP53 protein levels from (**C**) above. Mean ± SEM are shown alongside individual data points, colored by replicate (at least 3 replicates per condition, with all replicates shown in the graph). Data were normalized to siNT, then graphed and analyzed by ordinary one-way ANOVA with multiple comparisons against siNT and Holm-Šídák correction in GraphPad Prism 8. *****, $p < 0.05$; ******, $p < 0.01$; *******, $p < 0.001$.

(**E**). Log_2-scale RT-qPCR analysis of *CDKN1A* (*p21*) mRNA levels from control- or hit-treated MCF10A cells. The data from 3 biological replicates were normalized to the 7SL RNA abundance as a loading control, then to siNT for comparison using the $\Delta\Delta C_T$ method. Mean ± SEM are shown alongside individual data points, colored by replicate. Data were analyzed by ordinary one-way ANOVA with multiple comparisons against siNT and Holm-Šídák correction in GraphPad Prism 8. *****, $p < 0.05$; ******, $p < 0.01$; *******, $p < 0.001$.

Figure 7

A

hsa-miR-28-5p aAGGAGCUcacagucuauugag
hsa-miR-708-5p aAGGAGCUuacaaucuagcuggg

	hsa-miR-28-5p	hsa-miR-708-5p
MirGeneDB family	MIR-28	
One-nucleolus % effect	69.4	119.7
Nucleolar rRNA biogenesis % inhibition	none (less than 1% inhibition)	
% viability	22.9	10.6
Pre-rRNA processing phenotype	30S up, 21S strongly down	
18S/total RNA ratio, relative to siNT	0.582	0.542
Norm. puromycin levels, relative to siNT	72.0%	64.3%

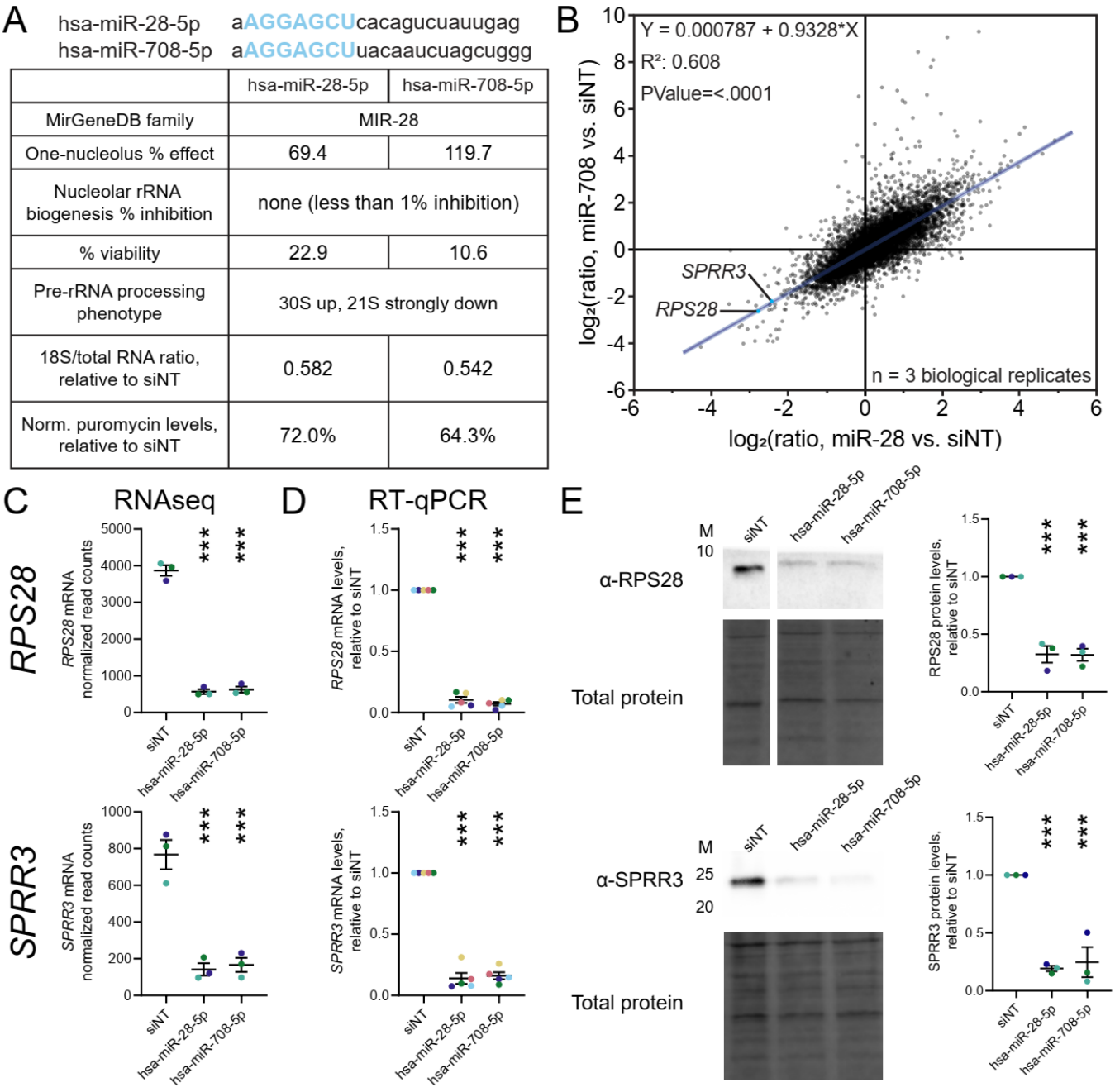

Figure 7. The MIR-28 siblings, hsa-miR-28-5p and hsa-miR-708-5p, directly target *RPS28* and downregulate *SPRR3*.

(**A**). Comparison of the MIR-28 family members, hsa-miR-28-5p and hsa-miR-708-5p. The full mature microRNA sequence is shown for each sibling, with the common AGGAGCU seed sequence indicated in blue. The table compares the RB phenotypes observed in MCF10A cells following treatment with either microRNA mimic.

(**B**). Regression comparing $\log_2$-scale RNAseq differential expression profiles of MCF10A cells treated with either hsa-miR-28-5p or hsa-miR-708-5p, relative to siNT negative control. Each dot represents one mRNA, with *RPS28* and *SPRR3* labeled. The line-of-best-fit shown in blue, with equation, R^2 value, and *p* value for non-zero slope indicated in top left. The data from 3 biological replicates were graphed and analyzed in JMP.

(**C**). Normalized RNAseq read counts mapping to *RPS28* or *SPRR3*. The mean ± SEM are shown alongside individual data points, colored by replicate (3 replicates). The data were analyzed by ordinary one-way ANOVA with multiple comparisons against siNT and Holm-Šídák correction in GraphPad Prism 8. *****, $p < 0.05$; ******, $p < 0.01$; *******, $p < 0.001$.

(**D**). RT-qPCR analysis of *RPS28* or *SPRR3* mRNA levels from control- or hit-treated MCF10A cells. The data were normalized to 7SL RNA abundance as a loading control, then to siNT for comparison using the $\Delta\Delta C_T$ method. Mean ± SEM are shown alongside individual data points, colored by replicate (5 replicates). The data were analyzed by ordinary one-way ANOVA with multiple comparisons against siNT and Holm-Šídák correction in GraphPad Prism 8. *****, $p < 0.05$; ******, $p < 0.01$; *******, $p < 0.001$.

(**E**). Immunoblot analysis and quantification of RPS28 or SPRR3 protein levels from control- or hit-treated MCF10A cells. α-RPS28 or α-SPRR3, indicates the example immunoblot for each protein. Total protein, trichloroethanol total protein stain loading control. M, molecular weight marker lane. The images were quantified with Bio-Rad Image Lab. Mean ± SEM are shown alongside individual data points, colored by replicate (3 replicates). The data were normalized to siNT, then graphed and analyzed by ordinary one-way ANOVA with multiple comparisons against siNT and Holm-Šídák correction in GraphPad Prism 8. *****, $p < 0.05$; ******, $p < 0.01$; *******, $p < 0.001$.

(**F**). Schematic for 3' UTR luciferase reporter assay for testing direct the binding of the MIR-28 siblings to *RPS28*. Diagram for the *RPS28* mRNA transcript, indicating untranslated regions (UTR; dark blue) or coding sequence (CDS; light blue). Putative MIR-28 binding sites 1 and 2 are shown in red, and their wild-type (WT) sequence is given along with the design for scrambled MIR-28 sites (SCR) rescue construct. WT or SCR regions of the *RPS28* 3' UTR containing both putative MIR-28 sites were cloned into the 3' UTR of the *Renilla* luciferase expression cassette in the psiCHECK2 plasmid.

(**G**). Quantification of 3' UTR luciferase reporter assays as in (**F**) testing direct binding of MIR-28 siblings to *RPS28*. The vector construct is indicated as wild-type (WT) or scrambled (SCR) above the transfection treatment labels. The luciferase data were collected for each treatment and construct combination, then normalized to the siNT treatment on a per-construct basis. Mean ± SEM are shown alongside individual data points, colored by replicate (5 replicates). The data were analyzed by unpaired two-sided Welch's *t*-tests between WT and SCR constructs in GraphPad Prism 8. *****, $p < 0.05$; ******, $p < 0.01$; *******, $p < 0.001$.

Figure 8

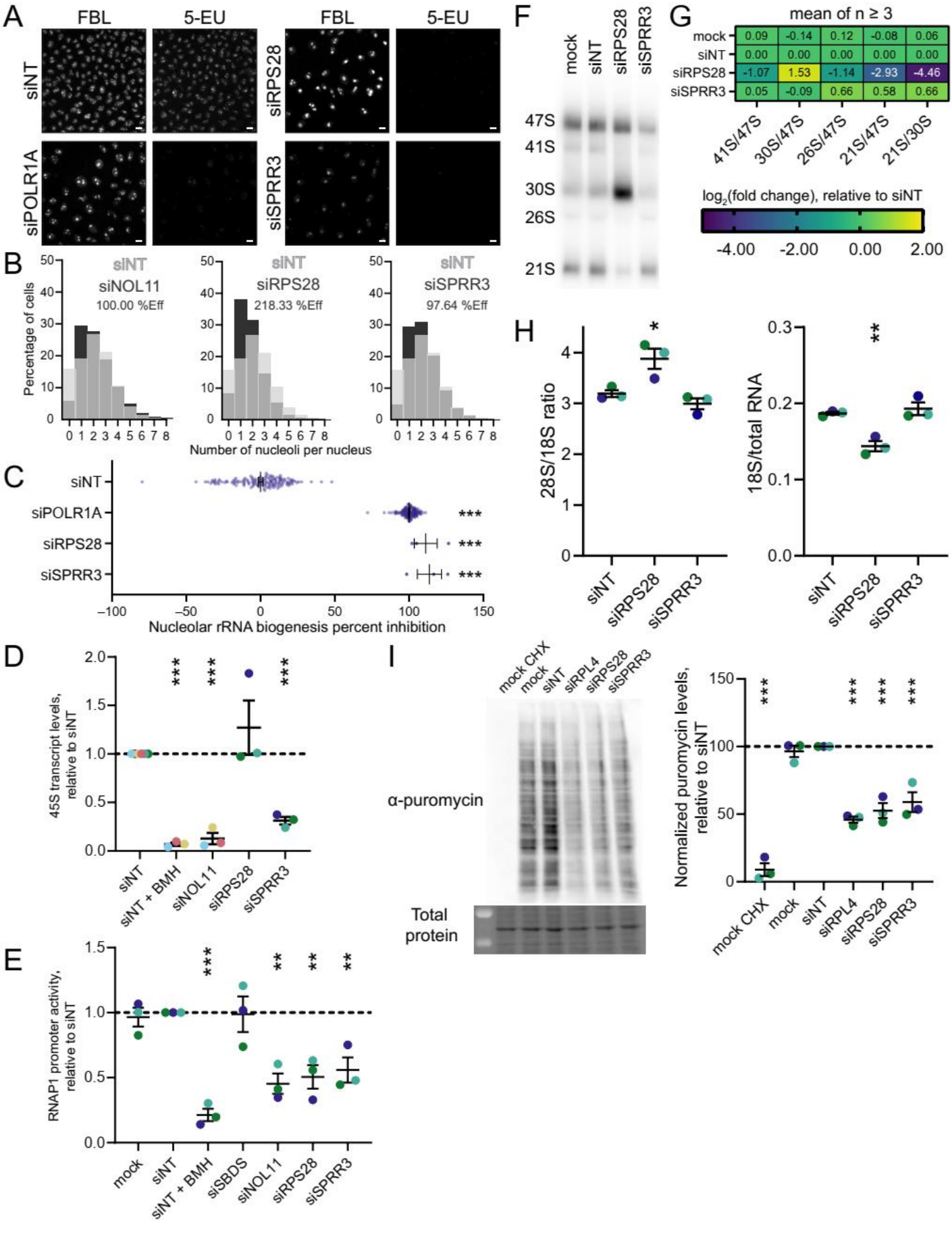

Figure 8. SPRR3 is a novel positive regulator of RNAP1 transcription.

(**A**). Representative images of control-treated, RPS28-depleted, or SPRR3-depleted MCF10A cells following fibrillarin (FBL) antibody staining and 5-EU incorporation. FBL immunostaining and 5-EU click labeling are shown as separate channels. Scale bars, 10 μm. siNT is a non-targeting negative control siRNA. siPOLR1A, POLR1A (RPA194) knockdown is a positive control.

(**B**) Quantification of nucleolar number following siRNA depletion of RPS28 or SPRR3. The histograms indicate the percentage of cells with a given number of nucleoli. The siNT negative control histogram is shown in light gray on all graphs for reference. Histograms from cells depleted of NOL11, RPS28, or SPRR3 are shown in black. siNOL11 is the positive control for decrease in nucleolar number. The one-nucleolus percent effect for black-labeled treatment is shown.

(**C**). Quantification of the percent inhibition of nucleolar rRNA biogenesis. The overall mean percent inhibition ± SEM is shown for each treatment, with each dot representing one well. The siNT negative control is set to 0% inhibition, and the siPOLR1A positive control is set to 100% inhibition. Data were analyzed by ordinary one-way ANOVA with multiple comparisons against siNT and Holm-Šídák correction in GraphPad Prism 8. *****, $p < 0.05$; ******, $p < 0.01$; *******, $p < 0.001$.

(**D**). RT-qPCR analysis of levels of the 45S pre-rRNA as a proxy for RNAP1 transcription. The mean ± SEM are shown alongside individual data points, colored by replicate (3 replicates). The data were normalized to 7SL RNA abundance as a loading control, then to siNT for comparison using the $\Delta\Delta C_T$ method. Data were analyzed by ordinary one-way ANOVA with multiple comparisons against siNT and Holm-Šídák correction in GraphPad Prism 8. *****, $p < 0.05$; ******, $p < 0.01$; *******, $p < 0.001$.

(**E**). Dual-luciferase reporter assay for RNAP1 promoter activity (47,94). The mean ± SEM are shown alongside individual data points, colored by replicate (3 replicates). The data were analyzed by ordinary one-way ANOVA with multiple comparisons against siNT and Holm-Šídák correction in GraphPad Prism 8. *****, $p < 0.05$; ******, $p < 0.01$; *******, $p < 0.001$.

(**F**). Representative ITS1 (probe P3) northern blot of 3 μg of total RNA isolated from RPS28- or SPRR3-depleted MCF10A cells. siNT is the non-targeting control. Mock is mock transfected. The pre-rRNA processing intermediates are labeled on the left. The pre-rRNA processing schematic is as in Figure 5A. The images were quantified using Bio-Rad Image Lab.

(**G**). Heatmap showing $\log_2$-transformed Ratio Analysis of Multiple Precursor [RAMP (76)] calculations, normalized to the si non-targeting (siNT) negative control. The values represent mean RAMP ratio for $n = 4$ replicates, except $n = 3$ for mock. RAMP ratios were calculated in Microsoft Excel and data were graphed in GraphPad Prism 8.

(**H**). Bioanalyzer analysis for 1 μg of total RNA isolated from RPS28- or SPRR3-depleted MCF10A cells. Left, the 28S/18S mature rRNA ratio; right, the 18S mature rRNA/total RNA ratio. Mean ± SEM are shown alongside individual data points, colored by replicate (3 replicates). The data were graphed and analyzed by ordinary one-way ANOVA with multiple comparisons against a non-targeting siRNA (siNT) and Holm-Šídák correction in GraphPad Prism 8. *****, $p < 0.05$; ******, $p < 0.01$; *******, $p < 0.001$.

(**I**). Representative examples of SUnSET puromycin incorporation assay (46,78) immunoblots of total protein isolated from RPS28 or SPRR3-depleted MCF10A cells. α-puromycin is an example blot for puromycin incorporation as a proxy for global protein synthesis. Total protein is the trichloroethanol total protein stain loading control. Mock CHX is mock cells treated with cycloheximide. Images were quantified with Bio-Rad Image Lab. The mean ± SEM are shown alongside individual data points, colored by replicate (3 replicates). siRPL4 is the positive control. Data were normalized to a non-

targeting siRNA (siNT), then graphed and analyzed by ordinary one-way ANOVA with multiple comparisons against siNT and Holm-Šídák correction in GraphPad Prism 8. *****, $p < 0.05$; ******, $p < 0.01$; *******, $p < 0.001$.

Supplementary Figure 1

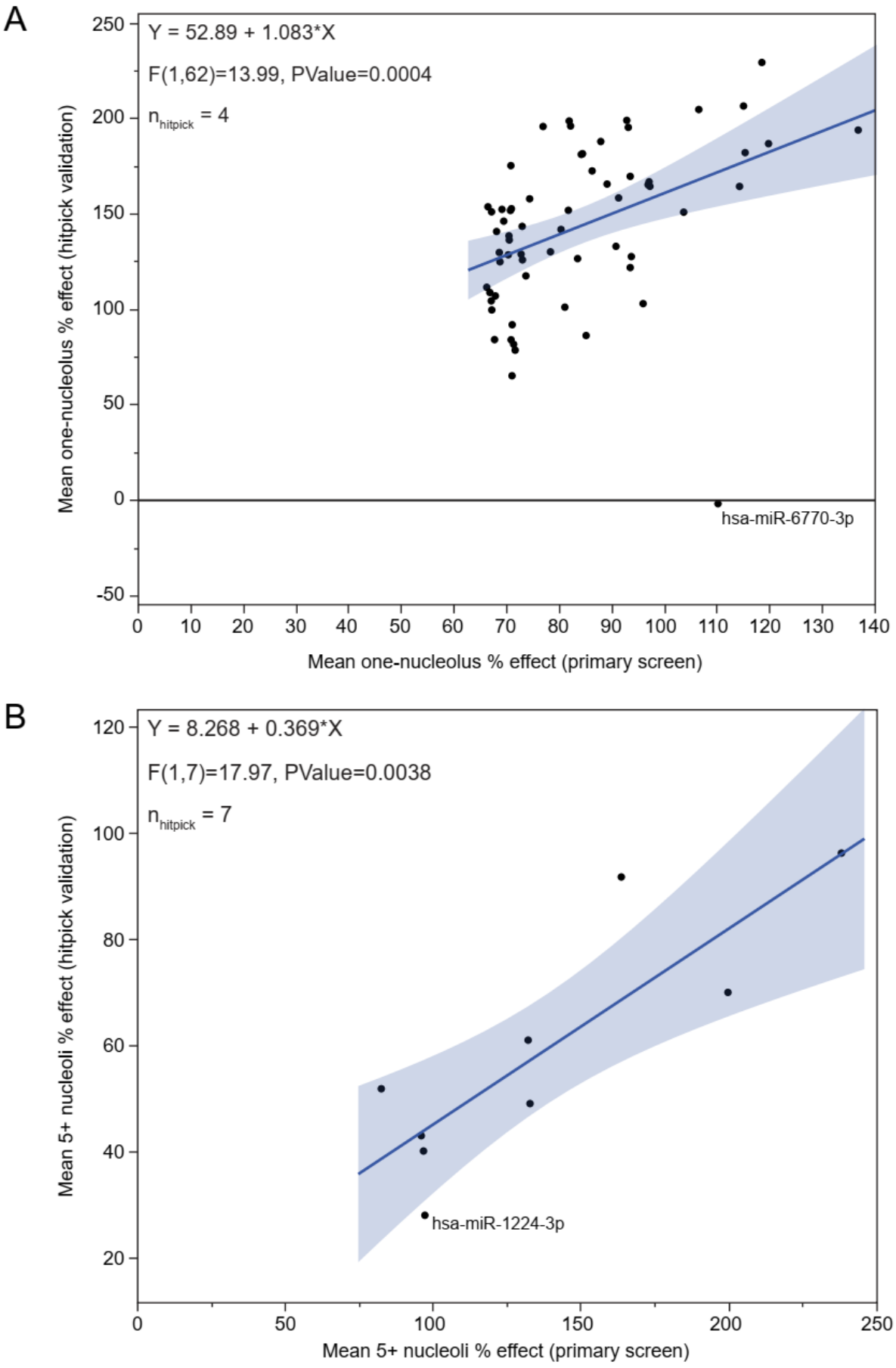

Supplementary Figure 1. Primary screen hitpick validation excludes hsa-miR-6770-3p and hsa-miR-1224-3p.

(**A**) Comparison of mean one-nucleolus percent effects from primary screen (x-axis) or hitpick validation (y-axis) for 64 one-nucleolus hits. One-nucleolus hitpick was conducted with $n = 4$ replicates. hsa-miR-6770-3p was excluded from downstream analysis.

(**B**) Comparison of mean 5+ nucleoli percent effects from primary screen (x-axis) or hitpick validation (y-axis) for nine 5+ nucleoli hits. 5+ nucleoli hitpick was conducted with $n = 7$ replicates. Graphing and linear regression was performed in JMP. hsa-miR-1224-3p was excluded from downstream analysis.

Supplementary Figure 2

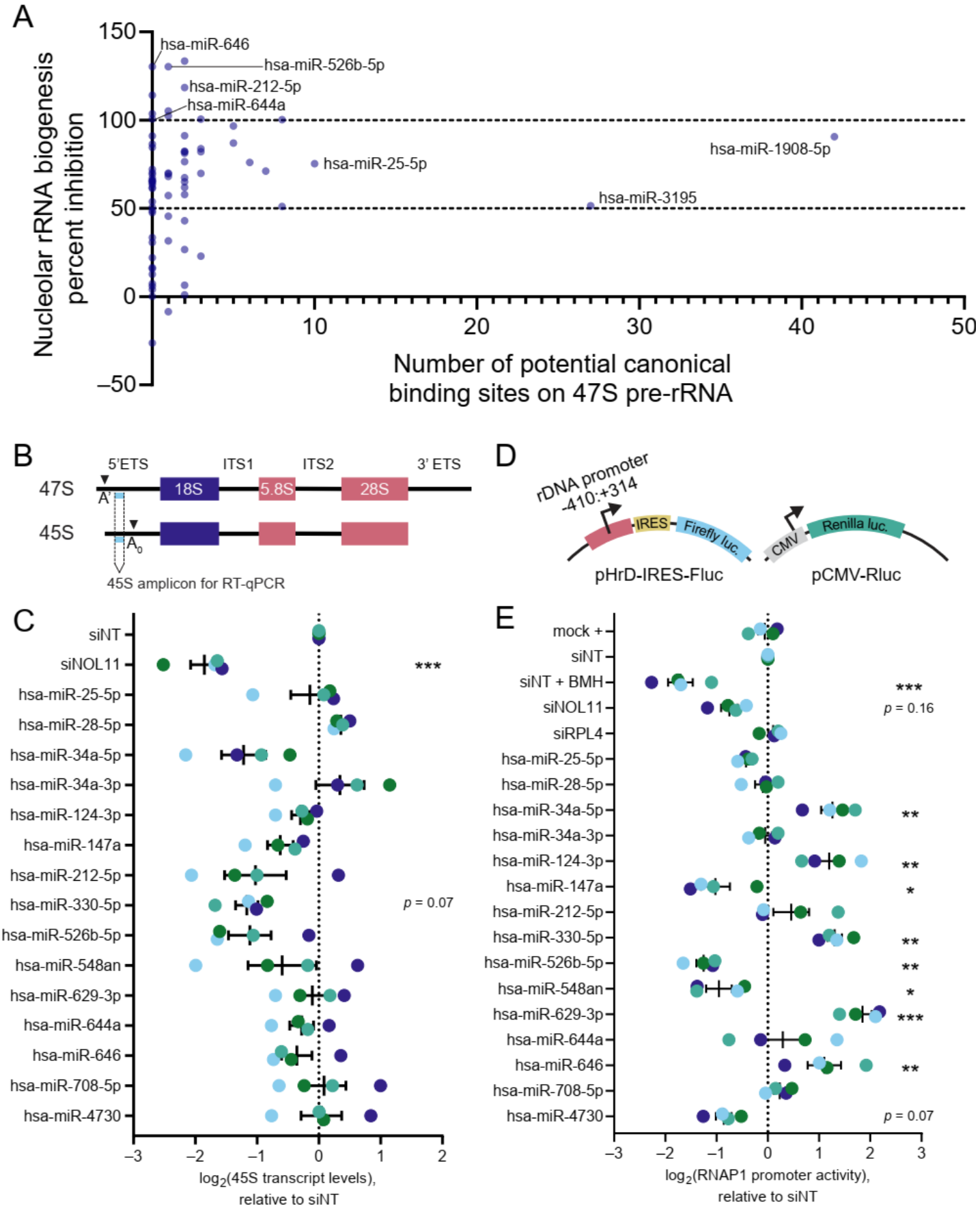

Supplementary Figure 2. MicroRNA hits do not reliably alter RNAP1 transcription.

(**A**). Scatter plot comparing the number of potential canonical (seed) binding sites on the 47S pre-rRNA transcript to the nucleolar rRNA biogenesis percent inhibition for the 72 microRNA hits, as predicted by BLAST. A number of hits have close to 0 predicted canonical 47S binding sites but strong nucleolar rRNA biogenesis percent inhibition. Select hits are labeled, and labels for percent inhibition are shown at 50% inhibition (empirical assay cutoff, consistent with pre-rRNA modification defect) and 100% inhibition (siPOLR1A positive control, consistent with pre-rRNA transcription defect) (54). The data were graphed in GraphPad Prism 8.

(**B**). Schematic indicating the amplicon (light blue) used for 45S pre-rRNA RT-qPCR, located between the A' and A_0 cleavage sites in the 5' ETS of the primary rRNA transcript. The location of the mature 18S, 5.8S and 28S rRNAs are indicated.

(**C**). RT-qPCR analysis of levels of the 45S pre-rRNA precursor transcript as a proxy for RNAP1 transcription. The mean ± SEM are shown alongside individual data points, colored by replicate (4 replicates). The data were normalized to 7SL RNA abundance as a loading control, then to siNT for comparison using the $\Delta\Delta C_T$ method. The data were analyzed by ordinary one-way ANOVA with multiple comparisons against siNT and Holm-Šídák correction in GraphPad Prism 8. *****, $p < 0.05$; ******, $p < 0.01$; *******, $p < 0.001$.

(**D**). Schematic for the dual-luciferase reporter assay for RNAP1 promoter activity (47,94). MCF10A cells were co-transfected with pHrD-IRES-Fluc, in which a 724 bp fragment of the rDNA promoter and early 5' ETS drive firefly luciferase production, and pCMV-Rluc, in which the constitutive CMV promoter drives *Renilla* luciferase production.

(**E**). Dual-luciferase reporter assay for RNAP1 promoter activity. The mean ± SEM are shown alongside individual data points, colored by replicate (4 replicates). The data were analyzed by ordinary one-way ANOVA with multiple comparisons against siNT and Holm-Šídák correction in GraphPad Prism 8. *****, $p < 0.05$; ******, $p < 0.01$; *******, $p < 0.001$.

Supplementary Figure 3

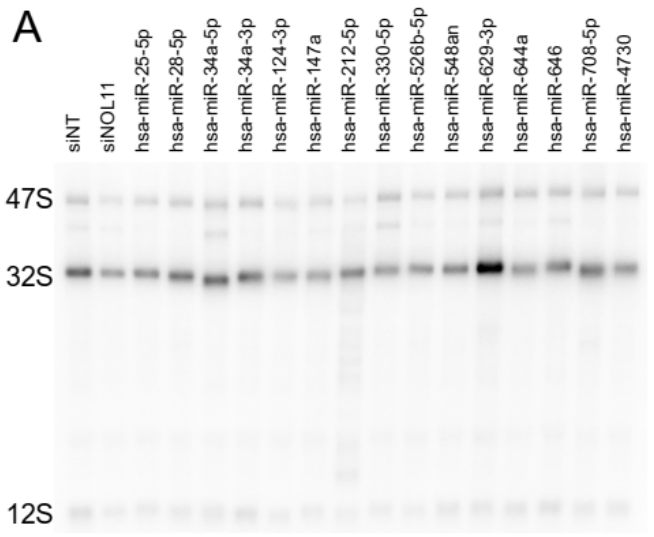

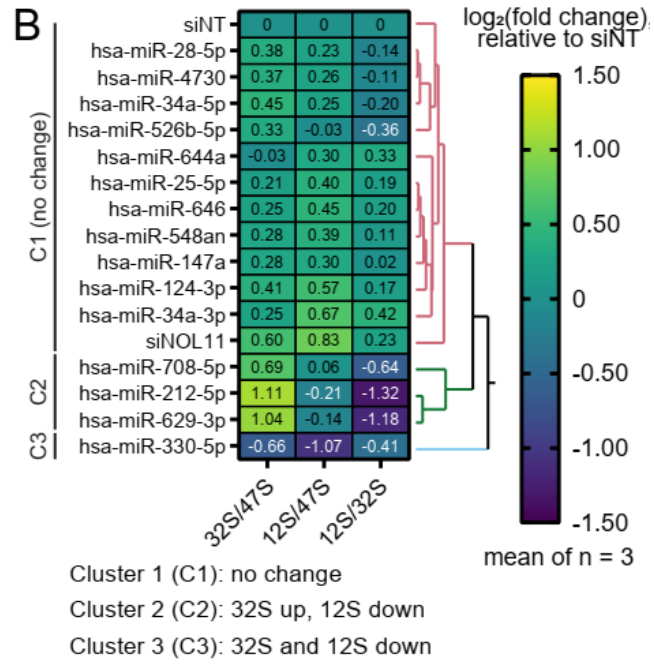

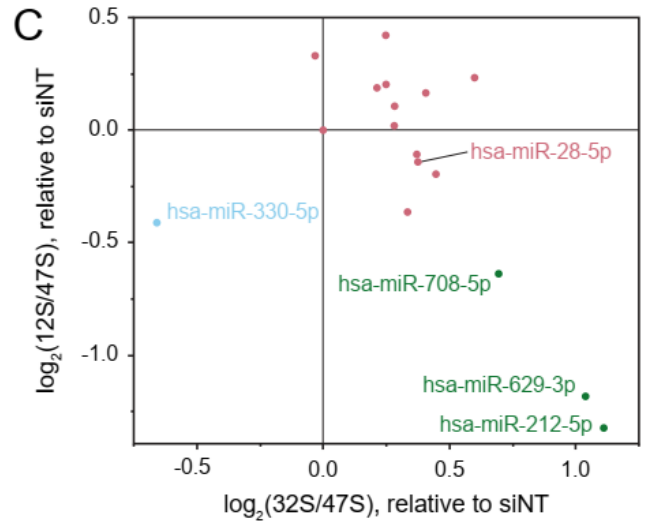

Supplementary Figure 3. Four microRNA hits slightly interfere with ITS2 processing.

(**A**). Representative ITS2 (probe P4) northern blot of 3 µg of total RNA isolated from control- or hit-treated MCF10A cells. The pre-rRNA processing intermediates are labeled on the left according to the schematic in Figure 5A. The images were quantified using Bio-Rad Image Lab.

(**B**). Clustered heatmap showing log_2-transformed Ratio Analysis of Multiple Precursor [RAMP, (76)] calculations for microRNA mimic hits, normalized to si non-targeting (siNT) negative control. Values represent mean log_2-scale RAMP ratio for n = 3 replicates. Clusters: no change (C1, red); 32S up, 12S down (C2, green); both 32S and 12S down (C3, blue). The RAMP ratios were calculated in Microsoft Excel. Three clusters were assigned using hierarchical Ward clustering in JMP, and data were graphed in GraphPad Prism 8.

(**C**). Log_2-scale 32S/47S and 12S/47S pre-rRNA precursor RAMP ratios after subset microRNA mimic treatment, relative to a non-targeting (siNT). Cluster colors the same as in (**B**). The data were graphed in GraphPad Prism 8, with select hits labeled.

Supplementary Figure 4

RPS28 3' UTR (NM_001031.5: 302-372)

hsa-miR-28-5p

A Site 1 (WT)

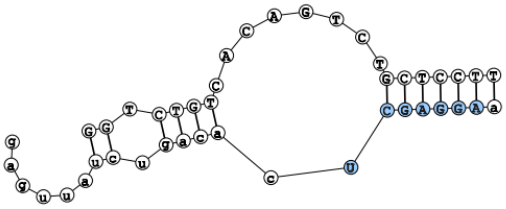

ENERGY = -13.4

E Site 1 (SCR)

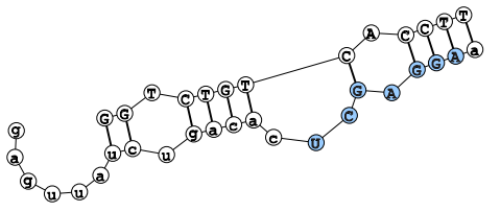

ENERGY = -7.1

B Site 2 (WT)

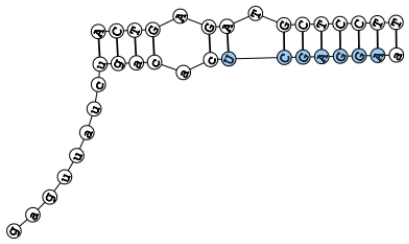

ENERGY = -16.1

F Site 2 (SCR)

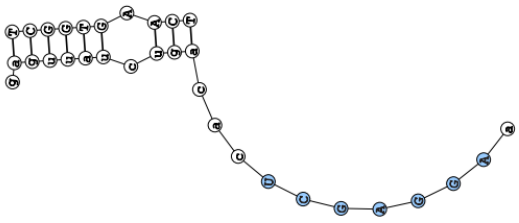

ENERGY = -5.8

hsa-miR-708-5p

C Site 1 (WT)

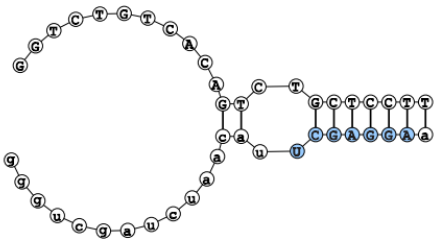

ENERGY = -12.5

G Site 1 (SCR)

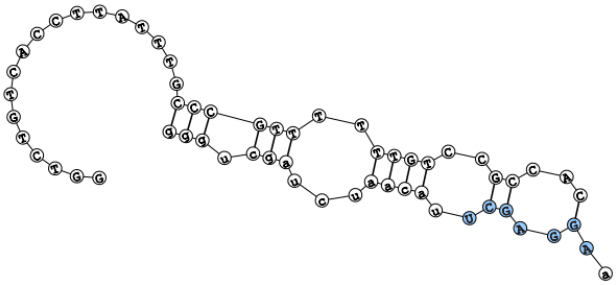

ENERGY = -10.0

D Site 2 (WT)

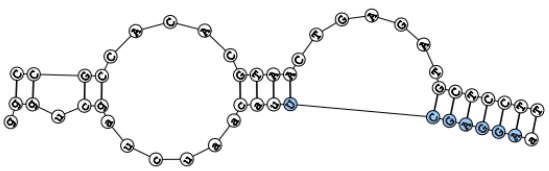

ENERGY = -12.6

H Site 2 (SCR)

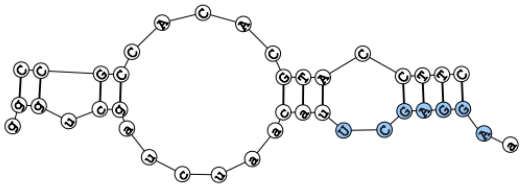

ENERGY = -6.3

Supplementary Figure 4. Predicted binding structures between MIR-28 siblings and putative binding sites in the *RPS28* 3' UTR.

(**A-D**). DuplexFold predicted structures between hsa-miR-28-5p (**A-B**) or hsa-miR-708-5p (**C-D**) to wild-type (WT) putative MIR-28 sites in the *RPS28* 3' untranslated region (UTR). The seed sequence for each microRNA is shown in blue. The DuplexFold predicted binding energies are indicated for each structure. Transcriptomic coordinates for the binding region input are shown in the header. Extraneous target base pairs were removed for visualization.

(**E-H**). Corresponding DuplexFold predicted structures between hsa-miR-28-5p (**E-F**) or hsa-miR-708-5p (**G-H**) to seed site scrambled (SCR) putative MIR-28 sites in *RPS28* 3' untranslated region (UTR). Each binding energy (red) is reduced following seed scrambling. Extraneous target base pairs were removed for visualization.

Supplementary Figure 5

SPRR3 5' UTR (NM_005416.3: 84-153)

A hsa-miR-28-5p

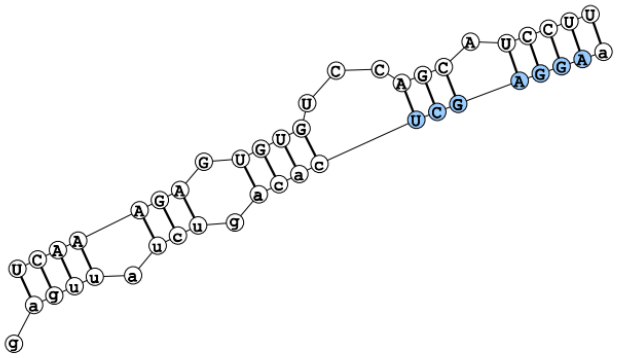

ENERGY = -18.9

B hsa-miR-708-5p

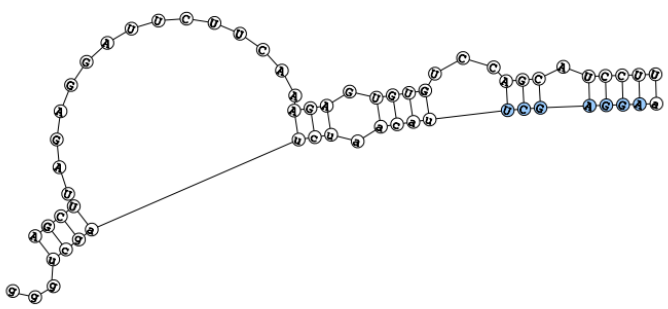

ENERGY = -13.6

SPRR3 CDS (NM_005416.3: 346-415)

C hsa-miR-28-5p

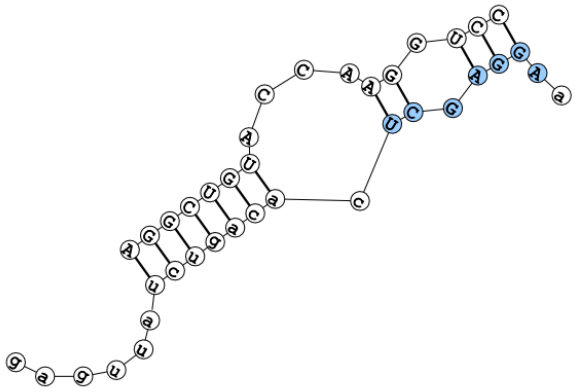

ENERGY = -13.7

D hsa-miR-708-5p

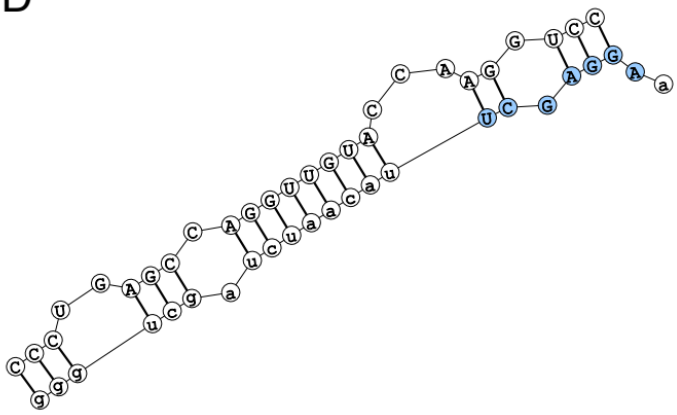

ENERGY = -21.1

E

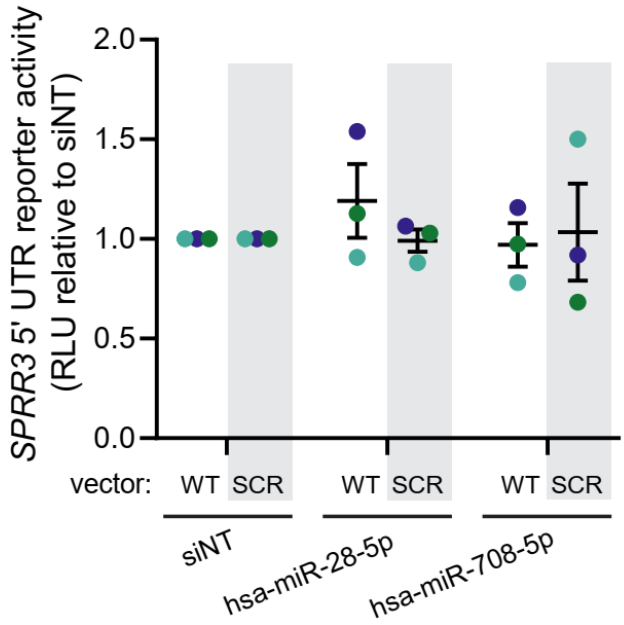

Supplementary Figure 5. MIR-28 siblings do not directly target the *SPRR3* 5' UTR.

(**A-B**). DuplexFold predicted structures between hsa-miR-28-5p (**A**) or hsa-miR-708-5p (**B**) to wild-type (WT) putative MIR-28 sites in the *SPRR3* 5' untranslated region (UTR). The seed sequence for each microRNA is shown in blue. The DuplexFold predicted binding energies are indicated for each structure. The transcriptomic coordinates for the binding region input are shown in the header. Extraneous target base pairs were removed for visualization.

(**C-D**). DuplexFold predicted structures between hsa-miR-28-5p (**C**) or hsa-miR-708-5p (**D**) to wild-type (WT) putative MIR-28 sites in the *SPRR3* coding sequence (CDS). The seeds do not appear to bind canonically. Other features as in (**A-B**).

(**E**). Quantification of luciferase reporter assays testing direct binding of MIR-28 siblings to the *SPRR3* 5' UTR. Vector construct indicated as wild-type (WT) or scrambled (SCR) above transfection treatment labels. Luciferase data were collected for each treatment and construct combination, then normalized to the non-targeting siRNA (siNT) treatment on a per-construct basis. The mean ± SEM are shown alongside individual data points, colored by replicate (3 replicates). The data were graphed in GraphPad Prism 8.

Supplementary Figure 6

A

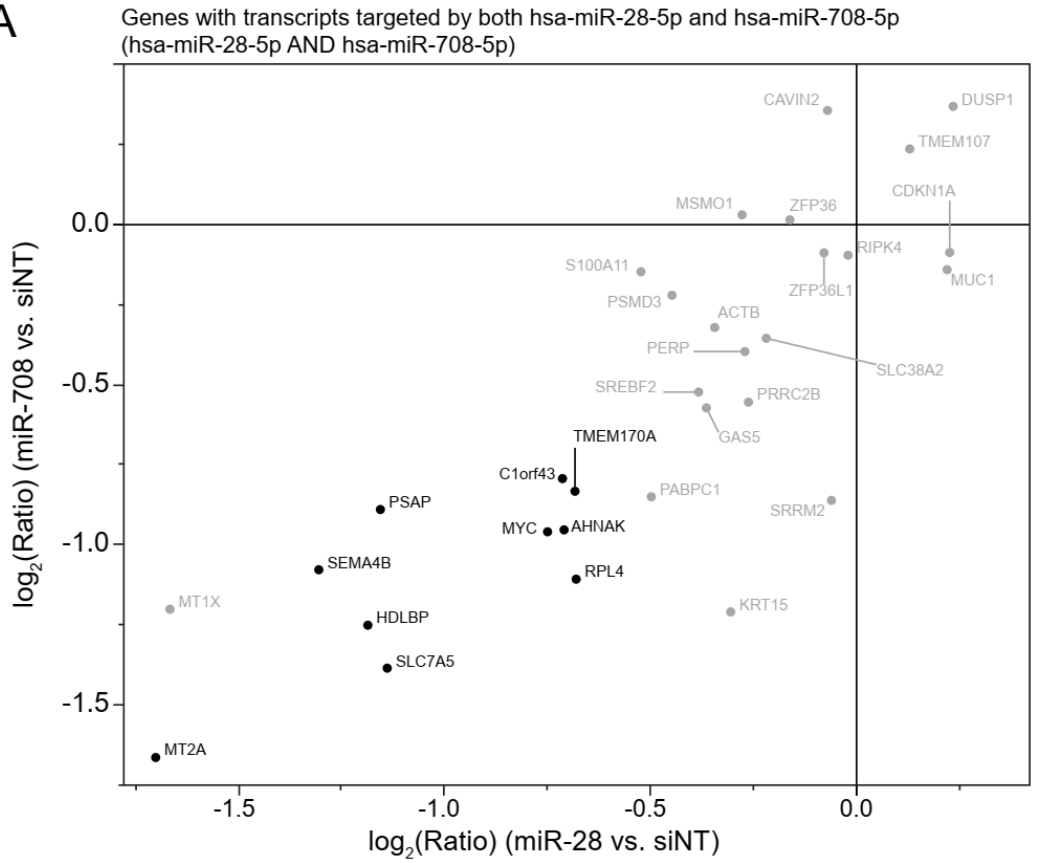

B

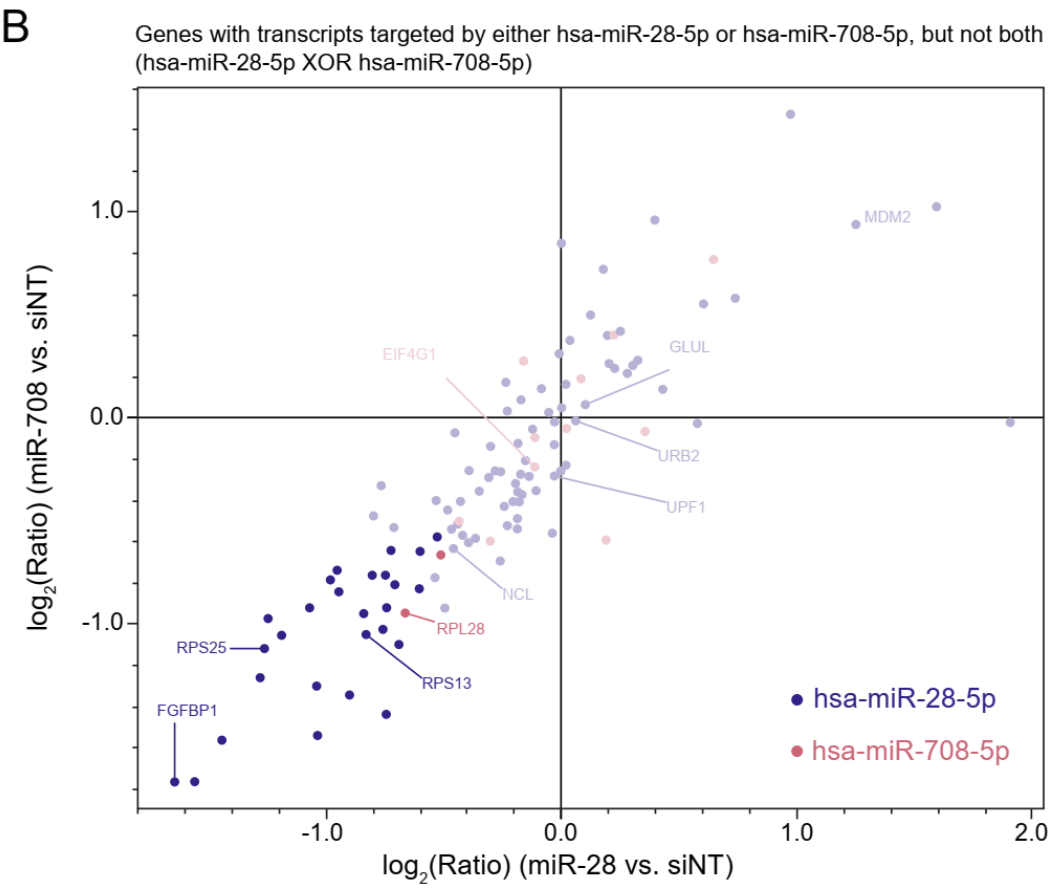

Supplementary Figure 6. Direct targets of the MIR-28 siblings revealed by miR-eCLIP.

(**A**). Plot of genes with mRNA transcripts targeted by both hsa-miR-28-5p and hsa-miR-708-5p. The miR-eCLIP data were filtered for genes expressed in MCF10A cells, and RNAseq differential expression data following MIR-28 treatment is graphed for each gene on the x- and y-axes. Bolded points represent genes downregulated by both MIR-28 mimics by at least -0.5 $\log_2$ units, with a differential expression false discovery rate < 0.05 for both treatments. All genes are labeled with their HGNC symbol.

(**B**). Plot of genes with mRNA transcripts targeted exclusively (XOR) by either hsa-miR-28-5p or hsa-miR-708-5p. The miR-eCLIP data were filtered and graphed as above. The genes encoding mRNA transcripts are colored blue if bound by hsa-miR-28-5p or red if bound by hsa-miR-708-5p, according to miR-eCLIP data. Select genes are labeled with HGNC symbol.

Supplementary Figure 7

MYC CDS (NM_002467.6:397-490)

A hsa-miR-28-5p

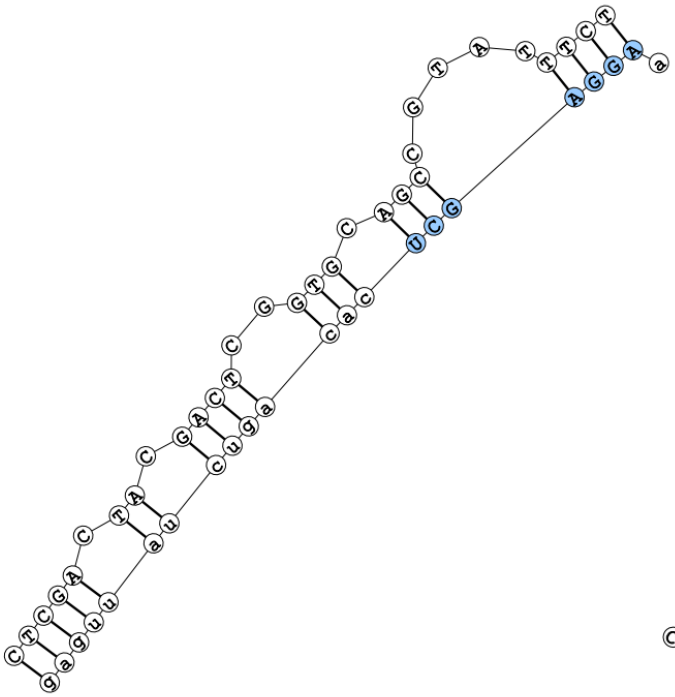

ENERGY = -13.0

B hsa-miR-708-5p

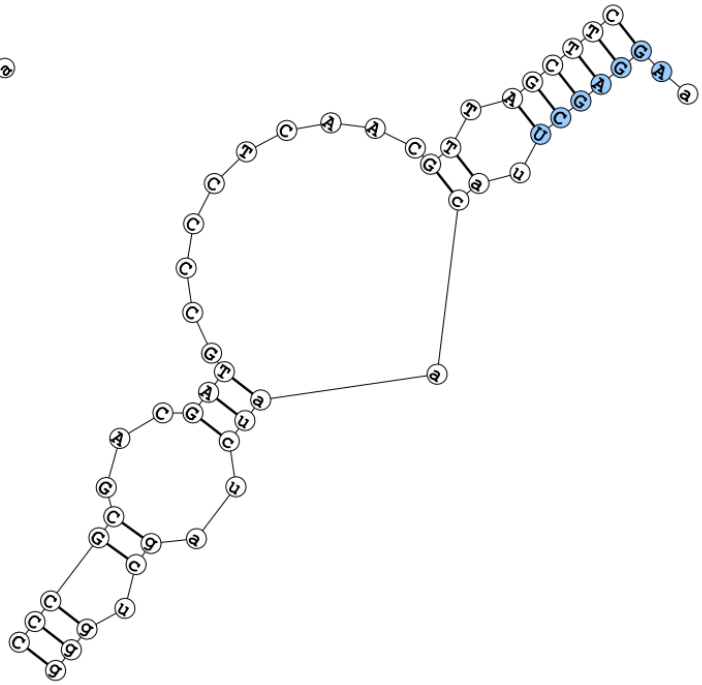

ENERGY = -12.7

CDKN1A 3' UTR (NM_000389.5:1986-2103)

C hsa-miR-28-5p

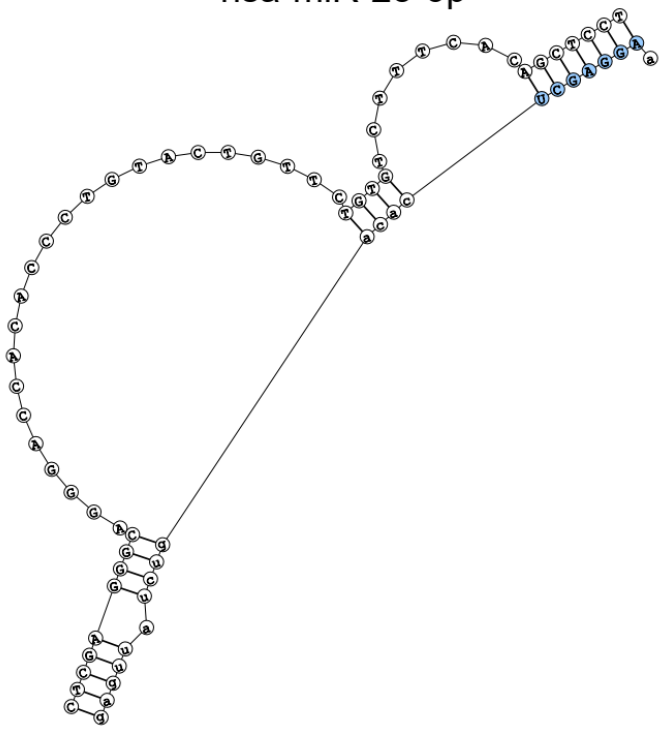

ENERGY = -16.6

D hsa-miR-708-5p

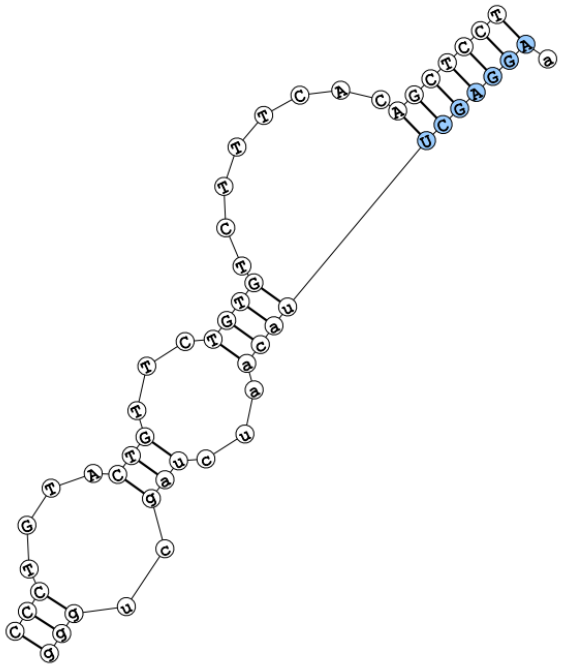

ENERGY = -15.3

Supplementary Figure 7. Predicted MIR-28 binding structures in the *MYC* CDS or *CDKN1A* (*p21*) 3' UTR.

(**A-B**). DuplexFold predicted structures between hsa-miR-28-5p (**A**) or hsa-miR-708-5p (**B**) and wild-type (WT) putative MIR-28 sites in the *MYC* coding sequence (CDS). The seed sequence for each microRNA is shown in blue. The DuplexFold predicted binding energies are indicated for each structure. Transcriptomic coordinates for the binding region input are shown in the header. Extraneous target base pairs were removed for visualization.

(**C-D**). DuplexFold predicted structures between hsa-miR-28-5p (**C**) or hsa-miR-708-5p (**D**) and wild-type (WT) putative MIR-28 sites in *CDKN1A* (*p21*) 3' UTR. Other features as in (**A-B**).

Supplementary Figure 8

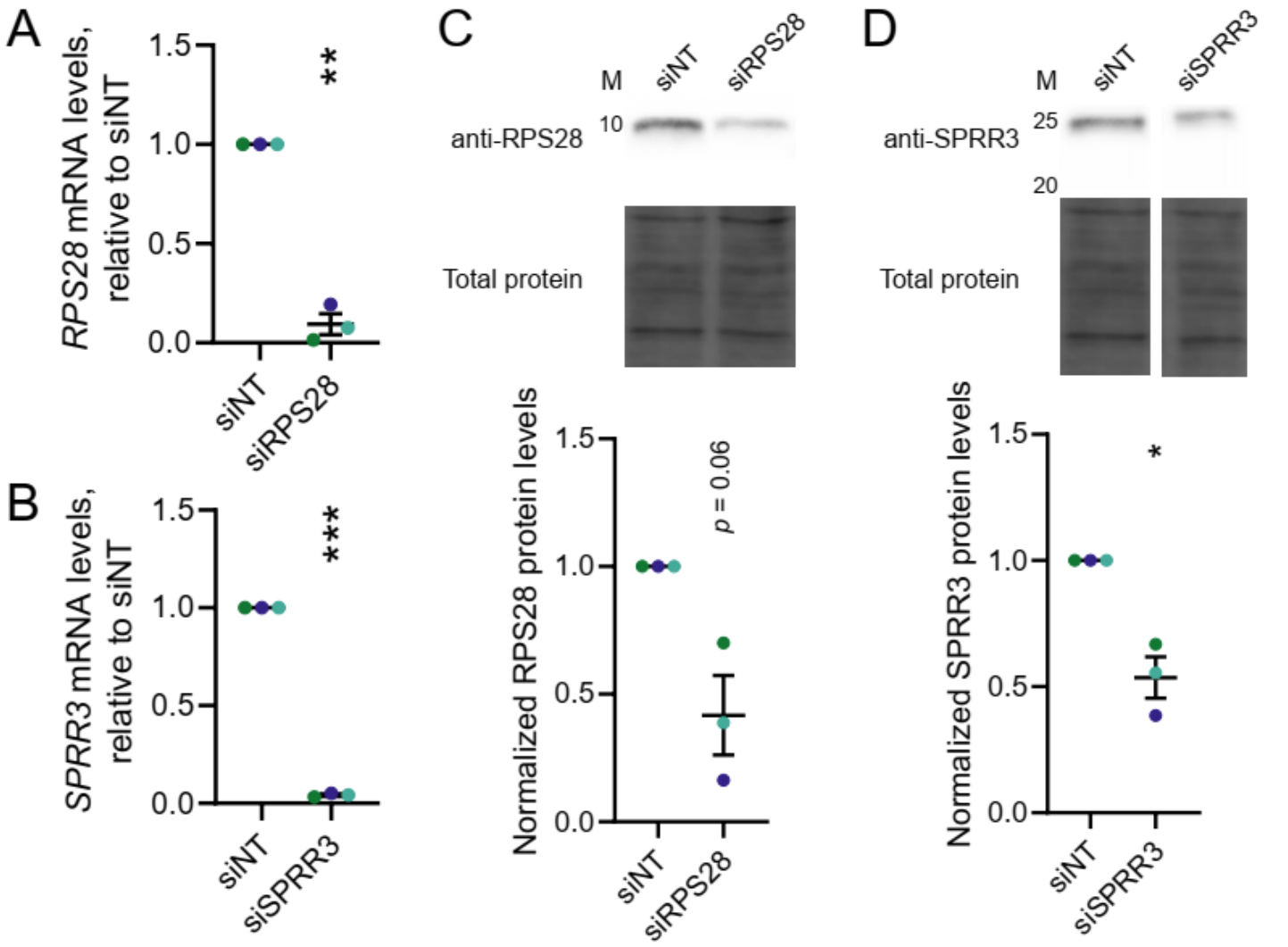

Supplementary Figure 8. Validation of siRNA-mediated knockdown of RPS28 or SPRR3.

(**A-B**) RT-qPCR quantification of mRNA transcript levels following siRNA knockdown for *RPS28* (**A**) or *SPRR3* (**B**). The data were normalized to the 7SL RNA abundance as a loading control, then to a non-targeting siRNA (siNT) for comparison using the $\Delta\Delta C_T$ method. The mean ± SEM are shown alongside individual data points, colored by replicate (3 replicates). Data were analyzed by unpaired two-sided Welch's *t*-tests in GraphPad Prism 8. *****, $p < 0.05$; ******, $p < 0.01$; *******, $p < 0.001$.

(**C-D**) Immunoblot quantification of protein levels following siRNA knockdown for *RPS28* (**C**) or *SPRR3* (**D**). Anti-RPS28 or anti-SPRR3 antibodies shown in example immunoblots for the indicated protein. Total protein is the trichloroethanol total protein stain loading control. M, molecular weight marker lane. The images were quantified using Bio-Rad Image Lab. The mean ± SEM are shown alongside individual data points, colored by replicate (3 replicates). The data were graphed and analyzed by unpaired two-sided Welch's *t*-tests in GraphPad Prism 8. *****, $p < 0.05$; ******, $p < 0.01$; *******, $p < 0.001$.

References

1. Lafontaine, D.L.J., Riback, J.A., Bascetin, R. and Brangwynne, C.P. (2021) The nucleolus as a multiphase liquid condensate. *Nat Rev Mol Cell Biol*, **22**, 165-182.
2. Bersaglieri, C. and Santoro, R. (2019) Genome organization in and around the nucleolus. *Cells*, **8**.
3. Correll, C.C., Bartek, J. and Dundr, M. (2019) The Nucleolus: A Multiphase Condensate Balancing Ribosome Synthesis and Translational Capacity in Health, Aging and Ribosomopathies. *Cells*, **8**.
4. Sharifi, S. and Bierhoff, H. (2018) Regulation of RNA Polymerase I Transcription in Development, Disease, and Aging. *Annu Rev Biochem*, **87**, 51-73.
5. Panov, K.I., Hannan, K., Hannan, R.D. and Hein, N. (2021) The Ribosomal Gene Loci-The Power behind the Throne. *Genes (Basel)*, **12**.
6. Moss, T., Mars, J.C., Tremblay, M.G. and Sabourin-Felix, M. (2019) The chromatin landscape of the ribosomal RNA genes in mouse and human. *Chromosome Res*.
7. Henras, A.K., Plisson-Chastang, C., O'Donohue, M.F., Chakraborty, A. and Gleizes, P.E. (2015) An overview of pre-ribosomal RNA processing in eukaryotes. *Wiley Interdiscip Rev RNA*, **6**, 225-242.
8. Lafontaine, D.L. (2015) Noncoding RNAs in eukaryotic ribosome biogenesis and function. *Nat Struct Mol Biol*, **22**, 11-19.
9. Bassler, J. and Hurt, E. (2019) Eukaryotic Ribosome Assembly. *Annu Rev Biochem*, **88**, 281-306.
10. Bohnsack, K.E. and Bohnsack, M.T. (2019) Uncovering the assembly pathway of human ribosomes and its emerging links to disease. *EMBO J*, **38**, e100278.
11. Klinge, S. and Woolford, J.L., Jr. (2019) Ribosome assembly coming into focus. *Nat Rev Mol Cell Biol*, **20**, 116-131.
12. Pena, C., Hurt, E. and Panse, V.G. (2017) Eukaryotic ribosome assembly, transport and quality control. *Nat Struct Mol Biol*, **24**, 689-699.
13. Espinar-Marchena, F.J., Babiano, R. and Cruz, J. (2017) Placeholder factors in ribosome biogenesis: please, pave my way. *Microb Cell*, **4**, 144-168.
14. Nerurkar, P., Altvater, M., Gerhardy, S., Schutz, S., Fischer, U., Weirich, C. and Panse, V.G. (2015) Eukaryotic Ribosome Assembly and Nuclear Export. *Int Rev Cell Mol Biol*, **319**, 107-140.
15. de la Cruz, J., Karbstein, K. and Woolford, J.L., Jr. (2015) Functions of ribosomal proteins in assembly of eukaryotic ribosomes in vivo. *Annu Rev Biochem*, **84**, 93-129.
16. Frazier, M.N., Pillon, M.C., Kocaman, S., Gordon, J. and Stanley, R.E. (2021) Structural overview of macromolecular machines involved in ribosome biogenesis. *Curr Opin Struct Biol*, **67**, 51-60.
17. James, A., Wang, Y., Raje, H., Rosby, R. and DiMario, P. (2014) Nucleolar stress with and without p53. *Nucleus*, **5**, 402-426.
18. Hannan, K.M., Soo, P., Wong, M.S., Lee, J.K., Hein, N., Evers, M., Wysoke, K.D., Williams, T.D., Montellese, C., Smith, L.K. *et al.* (2021) Nuclear stabilisation of p53 requires a functional nucleolar surveillance pathway. *bioRxiv*, 2021.2001.2021.427535.
19. Lafita-Navarro, M.C. and Conacci-Sorrell, M. (2022) Nucleolar stress: From development to cancer. *Semin Cell Dev Biol*.
20. Farley-Barnes, K.I., Ogawa, L.M. and Baserga, S.J. (2019) Ribosomopathies: Old Concepts, New Controversies. *Trends Genet*.
21. Mills, E.W. and Green, R. (2017) Ribosomopathies: There's strength in numbers. *Science*, **358**.

22. Armistead, J. and Triggs-Raine, B. (2014) Diverse diseases from a ubiquitous process: the ribosomopathy paradox. *Febs Lett*, **588**, 1491-1500.
23. Harold, C.M., Buhagiar, A.F., Cheng, Y. and Baserga, S.J. (2021) Ribosomal RNA Transcription Regulation in Breast Cancer. *Genes (Basel)*, **12**.
24. Catez, F., Dalla Venezia, N., Marcel, V., Zorbas, C., Lafontaine, D.L.J. and Diaz, J.J. (2019) Ribosome biogenesis: An emerging druggable pathway for cancer therapeutics. *Biochem Pharmacol*, **159**, 74-81.
25. Penzo, M., Montanaro, L., Trere, D. and Derenzini, M. (2019) The ribosome biogenesis-cancer connection. *Cells*, **8**.
26. Pelletier, J., Thomas, G. and Volarevic, S. (2018) Ribosome biogenesis in cancer: new players and therapeutic avenues. *Nat Rev Cancer*, **18**, 51-63.
27. Bustelo, X.R. and Dosil, M. (2018) Ribosome biogenesis and cancer: basic and translational challenges. *Curr Opin Genet Dev*, **48**, 22-29.
28. Sulima, S.O., Hofman, I.J.F., De Keersmaecker, K. and Dinman, J.D. (2017) How Ribosomes Translate Cancer. *Cancer Discov*, **7**, 1069-1087.
29. Zisi, A., Bartek, J. and Lindstrom, M.S. (2022) Targeting Ribosome Biogenesis in Cancer: Lessons Learned and Way Forward. *Cancers (Basel)*, **14**.
30. Bartel, D.P. (2018) Metazoan microRNAs. *Cell*, **173**, 20-51.
31. Gebert, L.F.R. and MacRae, I.J. (2019) Regulation of microRNA function in animals. *Nat Rev Mol Cell Biol*, **20**, 21-37.
32. Nakanishi, K. (2022) Anatomy of four human Argonaute proteins. *Nucleic Acids Res*.
33. Acunzo, M., Romano, G., Wernicke, D. and Croce, C.M. (2015) MicroRNA and cancer--a brief overview. *Adv Biol Regul*, **57**, 1-9.
34. Alvarez-Garcia, I. and Miska, E.A. (2005) MicroRNA functions in animal development and human disease. *Development*, **132**, 4653-4662.
35. McCool, M.A., Bryant, C.J. and Baserga, S.J. (2020) MicroRNAs and long non-coding RNAs as novel regulators of ribosome biogenesis. *Biochem Soc Trans*, **48**, 595-612.
36. Liang, X.H. and Crooke, S.T. (2011) Depletion of key protein components of the RISC pathway impairs pre-ribosomal RNA processing. *Nucleic Acids Res*, **39**, 4875-4889.
37. Atwood, B.L., Woolnough, J.L., Lefevre, G.M., Saint Just Ribeiro, M., Felsenfeld, G. and Giles, K.E. (2016) Human Argonaute 2 is tethered to ribosomal RNA through microRNA interactions. *J Biol Chem*, **291**, 17919-17928.
38. Bai, B., Liu, H. and Laiho, M. (2014) Small RNA expression and deep sequencing analyses of the nucleolus reveal the presence of nucleolus-associated microRNAs. *FEBS Open Bio*, **4**, 441-449.
39. Politz, J.C., Hogan, E.M. and Pederson, T. (2009) MicroRNAs with a nucleolar location. *RNA*, **15**, 1705-1715.
40. Li, Z.F., Liang, Y.M., Lau, P.N., Shen, W., Wang, D.K., Cheung, W.T., Xue, C.J., Poon, L.M. and Lam, Y.W. (2013) Dynamic localisation of mature microRNAs in Human nucleoli is influenced by exogenous genetic materials. *PLoS One*, **8**, e70869.
41. Reza, A. and Yuan, Y.G. (2021) microRNAs Mediated Regulation of the Ribosomal Proteins and its Consequences on the Global Translation of Proteins. *Cells*, **10**.
42. Bartel, D.P. (2009) MicroRNAs: target recognition and regulatory functions. *Cell*, **136**, 215-233.
43. Peterson, S.M., Thompson, J.A., Ufkin, M.L., Sathyanarayana, P., Liaw, L. and Congdon, C.B. (2014) Common features of microRNA target prediction tools. *Front Genet*, **5**, 23.
44. Zeng, X., Zhang, X. and Zou, Q. (2016) Integrative approaches for predicting microRNA function and prioritizing disease-related microRNA using biological interaction networks. *Brief Bioinform*, **17**, 193-203.
45. Pinzon, N., Li, B., Martinez, L., Sergeeva, A., Presumey, J., Apparailly, F. and Seitz, H. (2017) microRNA target prediction programs predict many false positives. *Genome Res*, **27**, 234-245.

46. Farley-Barnes, K.I., McCann, K.L., Ogawa, L.M., Merkel, J., Surovtseva, Y.V. and Baserga, S.J. (2018) Diverse Regulators of Human Ribosome Biogenesis Discovered by Changes in Nucleolar Number. *Cell Rep*, **22**, 1923-1934.
47. Ogawa, L.M., Buhagiar, A.F., Abriola, L., Leland, B.A., Surovtseva, Y.V. and Baserga, S.J. (2021) Increased numbers of nucleoli in a genome-wide RNAi screen reveal proteins that link the cell cycle to RNA polymerase I transcription. *Mol Biol Cell*, **32**, 956-973.
48. Wang, Y., Baskerville, S., Shenoy, A., Babiarz, J.E., Baehner, L. and Blelloch, R. (2008) Embryonic stem cell-specific microRNAs regulate the G1-S transition and promote rapid proliferation. *Nat Genet*, **40**, 1478-1483.
49. Olarerin-George, A.O., Anton, L., Hwang, Y.C., Elovitz, M.A. and Hogenesch, J.B. (2013) A functional genomics screen for microRNA regulators of NF-kappaB signaling. *BMC Biol*, **11**, 19.
50. Eulalio, A., Mano, M., Dal Ferro, M., Zentilin, L., Sinagra, G., Zacchigna, S. and Giacca, M. (2012) Functional screening identifies miRNAs inducing cardiac regeneration. *Nature*, **492**, 376-381.
51. Smith, J.L., Jeng, S., McWeeney, S.K. and Hirsch, A.J. (2017) A MicroRNA Screen Identifies the Wnt Signaling Pathway as a Regulator of the Interferon Response during Flavivirus Infection. *J Virol*, **91**.
52. Leivonen, S.K., Sahlberg, K.K., Makela, R., Due, E.U., Kallioniemi, O., Borresen-Dale, A.L. and Perala, M. (2014) High-throughput screens identify microRNAs essential for HER2 positive breast cancer cell growth. *Mol Oncol*, **8**, 93-104.
53. Nakano, H., Yamada, Y., Miyazawa, T. and Yoshida, T. (2013) Gain-of-function microRNA screens identify miR-193a regulating proliferation and apoptosis in epithelial ovarian cancer cells. *Int J Oncol*, **42**, 1875-1882.
54. Bryant, C.J., McCool, M.A., Abriola, L., Surovtseva, Y.V. and Baserga, S.J. (2022) A high-throughput assay for directly monitoring nucleolar rRNA biogenesis. *Open Biol*, **12**, 210305.
55. McCool, M.A., Buhagiar, A.F., Bryant, C.J., Ogawa, L.M., Abriola, L., Surovtseva, Y.V. and Baserga, S.J. (2022) Human pre-60S assembly factors link rRNA transcription to pre-rRNA processing. *RNA*.
56. Carpenter, A.E., Jones, T.R., Lamprecht, M.R., Clarke, C., Kang, I.H., Friman, O., Guertin, D.A., Chang, J.H., Lindquist, R.A., Moffat, J. *et al.* (2006) CellProfiler: image analysis software for identifying and quantifying cell phenotypes. *Genome Biol*, **7**, R100.
57. McQuin, C., Goodman, A., Chernyshev, V., Kamentsky, L., Cimini, B.A., Karhohs, K.W., Doan, M., Ding, L., Rafelski, S.M., Thirstrup, D. *et al.* (2018) CellProfiler 3.0: Next-generation image processing for biology. *PLoS Biol*, **16**, e2005970.
58. Zhang, X.D. (2011) Illustration of SSMD, z score, SSMD*, z* score, and t statistic for hit selection in RNAi high-throughput screens. *J Biomol Screen*, **16**, 775-785.
59. Hart, T., Komori, H.K., LaMere, S., Podshivalova, K. and Salomon, D.R. (2013) Finding the active genes in deep RNA-seq gene expression studies. *BMC Genomics*, **14**, 778.
60. Enuka, Y., Lauriola, M., Feldman, M.E., Sas-Chen, A., Ulitsky, I. and Yarden, Y. (2016) Circular RNAs are long-lived and display only minimal early alterations in response to a growth factor. *Nucleic Acids Res*, **44**, 1370-1383.
61. Tracy, K.M., Tye, C.E., Page, N.A., Fritz, A.J., Stein, J.L., Lian, J.B. and Stein, G.S. (2018) Selective expression of long non-coding RNAs in a breast cancer cell progression model. *J Cell Physiol*, **233**, 1291-1299.
62. Farley-Barnes, K.I., Deniz, E., Overton, M.M., Khokha, M.K. and Baserga, S.J. (2020) Paired Box 9 (PAX9), the RNA polymerase II transcription factor, regulates human ribosome biogenesis and craniofacial development. *PLoS Genet*, **16**, e1008967.
63. Thul, P.J., Akesson, L., Wiking, M., Mahdessian, D., Geladaki, A., Ait Blal, H., Alm, T., Asplund, A., Bjork, L., Breckels, L.M. *et al.* (2017) A subcellular map of the human proteome. *Science*, **356**.

64. Jarboui, M.A., Wynne, K., Elia, G., Hall, W.W. and Gautier, V.W. (2011) Proteomic profiling of the human T-cell nucleolus. *Mol Immunol*, **49**, 441-452.
65. Ahmad, Y., Boisvert, F.M., Gregor, P., Cobley, A. and Lamond, A.I. (2009) NOPdb: Nucleolar Proteome Database--2008 update. *Nucleic Acids Res*, **37**, D181-184.
66. Karagkouni, D., Paraskevopoulou, M.D., Chatzopoulos, S., Vlachos, I.S., Tastsoglou, S., Kanellos, I., Papadimitriou, D., Kavakiotis, I., Maniou, S., Skoufos, G. *et al.* (2018) DIANA-TarBase v8: a decade-long collection of experimentally supported miRNA-gene interactions. *Nucleic Acids Res*, **46**, D239-D245.
67. Xie, Z., Bailey, A., Kuleshov, M.V., Clarke, D.J.B., Evangelista, J.E., Jenkins, S.L., Lachmann, A., Wojciechowicz, M.L., Kropiwnicki, E., Jagodnik, K.M. *et al.* (2021) Gene Set Knowledge Discovery with Enrichr. *Curr Protoc*, **1**, e90.
68. Kuleshov, M.V., Jones, M.R., Rouillard, A.D., Fernandez, N.F., Duan, Q., Wang, Z., Koplev, S., Jenkins, S.L., Jagodnik, K.M., Lachmann, A. *et al.* (2016) Enrichr: a comprehensive gene set enrichment analysis web server 2016 update. *Nucleic Acids Res*, **44**, W90-97.
69. Chen, E.Y., Tan, C.M., Kou, Y., Duan, Q., Wang, Z., Meirelles, G.V., Clark, N.R. and Ma'ayan, A. (2013) Enrichr: interactive and collaborative HTML5 gene list enrichment analysis tool. *BMC Bioinformatics*, **14**, 128.
70. Love, M.I., Huber, W. and Anders, S. (2014) Moderated estimation of fold change and dispersion for RNA-seq data with DESeq2. *Genome Biol*, **15**, 550.
71. Woolnough, J.L., Atwood, B.L., Liu, Z., Zhao, R. and Giles, K.E. (2016) The Regulation of rRNA Gene Transcription during Directed Differentiation of Human Embryonic Stem Cells. *PLoS One*, **11**, e0157276.
72. Galiveti, C.R., Rozhdestvensky, T.S., Brosius, J., Lehrach, H. and Konthur, Z. (2010) Application of housekeeping npcRNAs for quantitative expression analysis of human transcriptome by real-time PCR. *RNA*, **16**, 450-461.
73. Hanashima, Y., Sano, E., Sumi, K., Ozawa, Y., Yagi, C., Tatsuoka, J., Yoshimura, S., Yamamuro, S., Ueda, T., Nakayama, T. *et al.* (2020) Antitumor effect of lenalidomide in malignant glioma cell lines. *Oncol Rep*, **43**, 1580-1590.
74. Wiza, C., Chadt, A., Blumensatt, M., Kanzleiter, T., Herzfeld De Wiza, D., Horrighs, A., Mueller, H., Nascimento, E.B., Schurmann, A., Al-Hasani, H. *et al.* (2014) Over-expression of PRAS40 enhances insulin sensitivity in skeletal muscle. *Arch Physiol Biochem*, **120**, 64-72.
75. de A Simão, T., Souza-Santos, P.T., de Oliveira, D.S., Bernardo, V., Lima, S.C., Rapozo, D.C., Kruel, C.D., Faria, P.A., Ribeiro Pinto, L.F. and Albano, R.M. (2011) Quantitative evaluation of SPRR3 expression in esophageal squamous cell carcinoma by qPCR and its potential use as a biomarker. *Exp Mol Pathol*, **91**, 584-589.
76. Wang, M., Anikin, L. and Pestov, D.G. (2014) Two orthogonal cleavages separate subunit RNAs in mouse ribosome biogenesis. *Nucleic Acids Res*, **42**, 11180-11191.
77. Ladner-Keay, C.L., Turner, R.J. and Edwards, R.A. (2018) Fluorescent Protein Visualization Immediately After Gel Electrophoresis Using an In-Gel Trichloroethanol Photoreaction with Tryptophan. *Methods Mol Biol*, **1853**, 179-190.
78. Schmidt, E.K., Clavarino, G., Ceppi, M. and Pierre, P. (2009) SUnSET, a nonradioactive method to monitor protein synthesis. *Nat Methods*, **6**, 275-277.
79. Agarwal, V., Bell, G.W., Nam, J.W. and Bartel, D.P. (2015) Predicting effective microRNA target sites in mammalian mRNAs. *Elife*, **4**.
80. Sticht, C., De La Torre, C., Parveen, A. and Gretz, N. (2018) miRWalk: An online resource for prediction of microRNA binding sites. *PLoS One*, **13**, e0206239.
81. Reuter, J.S. and Mathews, D.H. (2010) RNAstructure: software for RNA secondary structure prediction and analysis. *BMC Bioinformatics*, **11**, 129.
82. Sheu-Gruttadauria, J., Pawlica, P., Klum, S.M., Wang, S., Yario, T.A., Schirle Oakdale, N.T., Steitz, J.A. and MacRae, I.J. (2019) Structural Basis for Target-Directed MicroRNA Degradation. *Mol Cell*, **75**, 1243-1255 e1247.

83. Liu, H. and Naismith, J.H. (2008) An efficient one-step site-directed deletion, insertion, single and multiple-site plasmid mutagenesis protocol. *BMC Biotechnol*, **8**, 91.
84. Manakov, S.A., Shishkin, A.A., Yee, B.A., Shen, K.A., Cox, D.C., Park, S.S., Foster, H.M., Chapman, K.B., Yeo, G.W. and Van Nostrand, E.L. (2022) Scalable and deep profiling of mRNA targets for individual microRNAs with chimeric eCLIP. *bioRxiv*, 2022.2002.2013.480296.
85. Zhang, X.D. (2007) A new method with flexible and balanced control of false negatives and false positives for hit selection in RNA interference high-throughput screening assays. *J Biomol Screen*, **12**, 645-655.
86. Pfister, A.S. and Kuhl, M. (2018) Of Wnts and Ribosomes. *Prog Mol Biol Transl Sci*, **153**, 131-155.
87. Xiao, X., Gu, Y., Wang, G. and Chen, S. (2019) c-Myc, RMRP, and miR-34a-5p form a positive-feedback loop to regulate cell proliferation and apoptosis in multiple myeloma. *Int J Biol Macromol*, **122**, 526-537.
88. Goldfarb, K.C. and Cech, T.R. (2017) Targeted CRISPR disruption reveals a role for RNase MRP RNA in human preribosomal RNA processing. *Genes Dev*, **31**, 59-71.
89. Peltonen, K., Colis, L., Liu, H., Trivedi, R., Moubarek, M.S., Moore, H.M., Bai, B., Rudek, M.A., Bieberich, C.J. and Laiho, M. (2014) A targeting modality for destruction of RNA polymerase I that possesses anticancer activity. *Cancer Cell*, **25**, 77-90.
90. Peltonen, K., Colis, L., Liu, H., Jaamaa, S., Zhang, Z., Af Hallstrom, T., Moore, H.M., Sirajuddin, P. and Laiho, M. (2014) Small molecule BMH-compounds that inhibit RNA polymerase I and cause nucleolar stress. *Mol Cancer Ther*, **13**, 2537-2546.
91. Fromm, B., Hoye, E., Domanska, D., Zhong, X., Aparicio-Puerta, E., Ovchinnikov, V., Umu, S.U., Chabot, P.J., Kang, W., Aslanzadeh, M. *et al.* (2022) MirGeneDB 2.1: toward a complete sampling of all major animal phyla. *Nucleic Acids Res*, **50**, D204-D210.
92. Alles, J., Fehlmann, T., Fischer, U., Backes, C., Galata, V., Minet, M., Hart, M., Abu-Halima, M., Grasser, F.A., Lenhof, H.P. *et al.* (2019) An estimate of the total number of true human miRNAs. *Nucleic Acids Res*, **47**, 3353-3364.
93. Freed, E.F., Prieto, J.L., McCann, K.L., McStay, B. and Baserga, S.J. (2012) NOL11, implicated in the pathogenesis of North American Indian childhood cirrhosis, is required for pre-rRNA transcription and processing. *PLoS Genet*, **8**, e1002892.
94. Ghoshal, K., Majumder, S., Datta, J., Motiwala, T., Bai, S., Sharma, S.M., Frankel, W. and Jacob, S.T. (2004) Role of human ribosomal RNA (rRNA) promoter methylation and of methyl-CpG-binding protein MBD2 in the suppression of rRNA gene expression. *J Biol Chem*, **279**, 6783-6793.
95. Rubbi, C.P. and Milner, J. (2003) Disruption of the nucleolus mediates stabilization of p53 in response to DNA damage and other stresses. *EMBO J*, **22**, 6068-6077.
96. O'Donohue, M.F., Choesmel, V., Faubladier, M., Fichant, G. and Gleizes, P.E. (2010) Functional dichotomy of ribosomal proteins during the synthesis of mammalian 40S ribosomal subunits. *J Cell Biol*, **190**, 853-866.
97. Kim, H.K., Fuchs, G., Wang, S., Wei, W., Zhang, Y., Park, H., Roy-Chaudhuri, B., Li, P., Xu, J., Chu, K. *et al.* (2017) A transfer-RNA-derived small RNA regulates ribosome biogenesis. *Nature*, **552**, 57-62.
98. Kim, J.C., Yu, J.H., Cho, Y.K., Jung, C.S., Ahn, S.H., Gong, G., Kim, Y.S. and Cho, D.H. (2012) Expression of SPRR3 is associated with tumor cell proliferation in less advanced stages of breast cancer. *Breast Cancer Res Treat*, **133**, 909-916.
99. Yang, D., Li, R., Xia, J., Li, W., Ma, L., Ye, L. and Xue, H. (2020) Long Noncoding RNA PCAT18 Upregulates SPRR3 to Promote Colorectal Cancer Progression by Binding to miR-759. *Cancer Manag Res*, **12**, 11445-11452.
100. Cho, D.H., Jo, Y.K., Roh, S.A., Na, Y.S., Kim, T.W., Jang, S.J., Kim, Y.S. and Kim, J.C. (2010) Upregulation of SPRR3 promotes colorectal tumorigenesis. *Mol Med*, **16**, 271-277.

101. Wu, M., Guo, Q., Liu, X. and Wu, L. (2022) SPRR3, a novel miR-338-3p target, regulates the malignant progression of clear cell renal cell carcinoma in vitro via the PI3K/Akt signaling pathway. *Exp Ther Med*, **23**, 317.
102. Liu, Q., Zhang, C., Ma, G. and Zhang, Q. (2014) Expression of SPRR3 is associated with tumor cell proliferation and invasion in glioblastoma multiforme. *Oncol Lett*, **7**, 427-432.
103. Li, Q., Wang, Y., Hu, R. and Yang, G. (2020) Dysregulation of SPRR3/miR-876-3p Axis Contributes to Tumorigenesis in Non-Small-Cell Lung Cancer. *Onco Targets Ther*, **13**, 2411-2419.
104. Hu, X., Peng, N., Qi, F., Li, J., Shi, L. and Chen, R. (2018) Cigarette smoke upregulates SPRR3 by favoring c-Jun/Fra1 heterodimerization in human bronchial epithelial cells. *Future Oncol*, **14**, 2599-2613.
105. Bae, J.E., Choi, H., Shin, D.W., Na, H.W., Park, N.Y., Kim, J.B., Jo, D.S., Cho, M.J., Lyu, J.H., Chang, J.H. *et al.* (2019) Fine particulate matter (PM2.5) inhibits ciliogenesis by increasing SPRR3 expression via c-Jun activation in RPE cells and skin keratinocytes. *Sci Rep*, **9**, 3994.
106. Jin, Y., Chen, Z., Liu, X. and Zhou, X. (2013) Evaluating the microRNA targeting sites by luciferase reporter gene assay. *Methods Mol Biol*, **936**, 117-127.
107. Piazzi, M., Bavelloni, A., Gallo, A., Faenza, I. and Blalock, W.L. (2019) Signal Transduction in Ribosome Biogenesis: A Recipe to Avoid Disaster. *Int J Mol Sci*, **20**.
108. Politz, J.C., Zhang, F. and Pederson, T. (2006) MicroRNA-206 colocalizes with ribosome-rich regions in both the nucleolus and cytoplasm of rat myogenic cells. *Proc Natl Acad Sci U S A*, **103**, 18957-18962.
109. Reyes-Gutierrez, P., Ritland Politz, J.C. and Pederson, T. (2014) A mRNA and cognate microRNAs localize in the nucleolus. *Nucleus*, **5**, 636-642.
110. Jin, H.Y., Gonzalez-Martin, A., Miletic, A.V., Lai, M., Knight, S., Sabouri-Ghomi, M., Head, S.R., Macauley, M.S., Rickert, R.C. and Xiao, C. (2015) Transfection of microRNA Mimics Should Be Used with Caution. *Front Genet*, **6**, 340.
111. Khan, A.A., Betel, D., Miller, M.L., Sander, C., Leslie, C.S. and Marks, D.S. (2009) Transfection of small RNAs globally perturbs gene regulation by endogenous microRNAs. *Nat Biotechnol*, **27**, 549-555.
112. Sood, P., Krek, A., Zavolan, M., Macino, G. and Rajewsky, N. (2006) Cell-type-specific signatures of microRNAs on target mRNA expression. *Proc Natl Acad Sci U S A*, **103**, 2746-2751.
113. Dörner, K., Badertscher, L., Horvath, B., Hollandi, R., Molnar, C., Fuhrer, T., Meier, R., Sarazova, M., van den Heuvel, J., Zamboni, N. *et al.* (2022) Genome-wide RNAi screen identifies novel players in human 60S subunit biogenesis including key enzymes of polyamine metabolism. *Nucleic Acids Res*, **50**, 2872-2888.
114. Badertscher, L., Wild, T., Montellese, C., Alexander, L.T., Bammert, L., Sarazova, M., Stebler, M., Csucs, G., Mayer, T.U., Zamboni, N. *et al.* (2015) Genome-wide RNAi Screening Identifies Protein Modules Required for 40S Subunit Synthesis in Human Cells. *Cell Rep*, **13**, 2879-2891.
115. Tafforeau, L., Zorbas, C., Langhendries, J.L., Mullineux, S.T., Stamatopoulou, V., Mullier, R., Wacheul, L. and Lafontaine, D.L. (2013) The complexity of human ribosome biogenesis revealed by systematic nucleolar screening of Pre-rRNA processing factors. *Mol Cell*, **51**, 539-551.
116. Engeland, K. (2022) Cell cycle regulation: p53-p21-RB signaling. *Cell Death Differ*, **29**, 946-960.
117. Wu, S., Huang, S., Ding, J., Zhao, Y., Liang, L., Liu, T., Zhan, R. and He, X. (2010) Multiple microRNAs modulate p21Cip1/Waf1 expression by directly targeting its 3' untranslated region. *Oncogene*, **29**, 2302-2308.
118. Zhu, S., He, C., Deng, S., Li, X., Cui, S., Zeng, Z., Liu, M., Zhao, S., Chen, J., Jin, Y. *et al.* (2016) MiR-548an, Transcriptionally Downregulated by HIF1alpha/HDAC1, Suppresses

Tumorigenesis of Pancreatic Cancer by Targeting Vimentin Expression. *Mol Cancer Ther*, **15**, 2209-2219.
119. Yang, W., Ju, H.Y. and Tian, X.F. (2020) Hsa-miR-4730 as a new and potential diagnostic and prognostic indicators for pancreatic cancer. *Eur Rev Med Pharmacol Sci*, **24**, 8801-8811.
120. Yata, K., Beder, L.B., Tamagawa, S., Hotomi, M., Hirohashi, Y., Grenman, R. and Yamanaka, N. (2015) MicroRNA expression profiles of cancer stem cells in head and neck squamous cell carcinoma. *Int J Oncol*, **47**, 1249-1256.
121. Sanchez-Diaz, P.C., Hsiao, T.H., Chang, J.C., Yue, D., Tan, M.C., Chen, H.I., Tomlinson, G.E., Huang, Y., Chen, Y. and Hung, J.Y. (2013) De-regulated microRNAs in pediatric cancer stem cells target pathways involved in cell proliferation, cell cycle and development. *PLoS One*, **8**, e61622.
122. Liu, H., Chen, W., Zhi, X., Chen, E.J., Wei, T., Zhang, J., Shen, J., Hu, L.Q., Zhao, B., Feng, X.H. *et al.* (2018) Tumor-derived exosomes promote tumor self-seeding in hepatocellular carcinoma by transferring miRNA-25-5p to enhance cell motility. *Oncogene*, **37**, 4964-4978.
123. Cheng, L., Wang, H. and Han, S. (2017) MiR-3910 Promotes the Growth and Migration of Cancer Cells in the Progression of Hepatocellular Carcinoma. *Dig Dis Sci*, **62**, 2812-2820.
124. Uhlmann, S., Mannsperger, H., Zhang, J.D., Horvat, E.A., Schmidt, C., Kublbeck, M., Henjes, F., Ward, A., Tschulena, U., Zweig, K. *et al.* (2012) Global microRNA level regulation of EGFR-driven cell-cycle protein network in breast cancer. *Mol Syst Biol*, **8**, 570.
125. Zhang, Y., Zhang, H.E. and Liu, Z. (2016) MicroRNA-147 suppresses proliferation, invasion and migration through the AKT/mTOR signaling pathway in breast cancer. *Oncol Lett*, **11**, 405-410.
126. Lu, Y. and Luan, X.R. (2020) miR-147a suppresses the metastasis of non-small-cell lung cancer by targeting CCL5. *J Int Med Res*, **48**, 300060519883098.
127. Raza, U., Saatci, O., Uhlmann, S., Ansari, S.A., Eyupoglu, E., Yurdusev, E., Mutlu, M., Ersan, P.G., Altundag, M.K., Zhang, J.D. *et al.* (2016) The miR-644a/CTBP1/p53 axis suppresses drug resistance by simultaneous inhibition of cell survival and epithelial-mesenchymal transition in breast cancer. *Oncotarget*, **7**, 49859-49877.
128. Li, Y., Yan, X., Ren, L. and Li, Y. (2018) miR-644a Inhibits Cellular Proliferation and Invasion via Suppression of CtBP1 in Gastric Cancer Cells. *Oncol Res*, **26**, 1-8.
129. Pang, J., Li, Z., Wang, G., Li, N., Gao, Y. and Wang, S. (2018) miR-214-5p targets KLF5 and suppresses proliferation of human hepatocellular carcinoma cells. *J Cell Biochem*.
130. Zhang, M., Wang, D., Zhu, T. and Yin, R. (2017) miR-214-5p Targets ROCK1 and Suppresses Proliferation and Invasion of Human Osteosarcoma Cells. *Oncol Res*, **25**, 75-81.
131. Yamaguchi, N., Osaki, M., Onuma, K., Yumioka, T., Iwamoto, H., Sejima, T., Kugoh, H., Takenaka, A. and Okada, F. (2017) Identification of MicroRNAs Involved in Resistance to Sunitinib in Renal Cell Carcinoma Cells. *Anticancer Res*, **37**, 2985-2992.
132. Wu, X., Cheng, Y.L., Matthen, M., Yoon, A., Schwartz, G.K., Bala, S., Taylor, A.M. and Momen-Heravi, F. (2021) Down-regulation of the tumor suppressor miR-34a contributes to head and neck cancer by up-regulating the MET oncogene and modulating tumor immune evasion. *J Exp Clin Cancer Res*, **40**, 70.
133. Meng, F. and Zhang, L. (2019) miR-183-5p functions as a tumor suppressor in lung cancer through PIK3CA inhibition. *Exp Cell Res*, **374**, 315-322.
134. Cheng, Y., Xiang, G., Meng, Y. and Dong, R. (2016) MiRNA-183-5p promotes cell proliferation and inhibits apoptosis in human breast cancer by targeting the PDCD4. *Reprod Biol*, **16**, 225-233.
135. Yan, H., Sun, B.M., Zhang, Y.Y., Li, Y.J., Huang, C.X., Feng, F.Z. and Li, C. (2018) Upregulation of miR-183-5p is responsible for the promotion of apoptosis and inhibition of the epithelial-mesenchymal transition, proliferation, invasion and migration of human endometrial cancer cells by downregulating Ezrin. *Int J Mol Med*, **42**, 2469-2480.

136. He, R.Q., Gao, L., Ma, J., Li, Z.Y., Hu, X.H. and Chen, G. (2018) Oncogenic role of miR-183-5p in lung adenocarcinoma: A comprehensive study of qPCR, in vitro experiments and bioinformatic analysis. *Oncol Rep*, **40**, 83-100.
137. Liu, W., Wang, D., Wang, X., Liu, P. and Yan, M. (2020) hsa_circ_0085539 Promotes Osteosarcoma Progression by Regulating miR-526b-5p and SERP1. *Mol Ther Oncolytics*, **19**, 163-177.
138. Zhou, Y.X., Wang, C., Mao, L.W., Wang, Y.L., Xia, L.Q., Zhao, W., Shen, J. and Chen, J. (2018) Long noncoding RNA HOTAIR mediates the estrogen-induced metastasis of endometrial cancer cells via the miR-646/NPM1 axis. *Am J Physiol Cell Physiol*, **314**, C690-C701.
139. Zhang, P., Tang, W.M., Zhang, H., Li, Y.Q., Peng, Y., Wang, J., Liu, G.N., Huang, X.T., Zhao, J.J., Li, G. *et al.* (2017) MiR-646 inhibited cell proliferation and EMT-induced metastasis by targeting FOXK1 in gastric cancer. *Br J Cancer*, **117**, 525-534.
140. Zo, R.B. and Long, Z. (2018) MiR-124-3p suppresses bladder cancer by targeting DNA methyltransferase 3B. *J Cell Physiol*, **234**, 464-474.
141. Wang, Y., Chen, L., Wu, Z., Wang, M., Jin, F., Wang, N., Hu, X., Liu, Z., Zhang, C.Y., Zen, K. *et al.* (2016) miR-124-3p functions as a tumor suppressor in breast cancer by targeting CBL. *BMC Cancer*, **16**, 826.
142. Lwin, T., Zhao, X., Cheng, F., Zhang, X., Huang, A., Shah, B., Zhang, Y., Moscinski, L.C., Choi, Y.S., Kozikowski, A.P. *et al.* (2013) A microenvironment-mediated c-Myc/miR-548m/HDAC6 amplification loop in non-Hodgkin B cell lymphomas. *J Clin Invest*, **123**, 4612-4626.
143. Mansoori, B., Mohammadi, A., Naghizadeh, S., Gjerstorff, M., Shanehbandi, D., Shirjang, S., Najafi, S., Holmskov, U., Khaze, V., Duijf, P.H.G. *et al.* (2020) miR-330 suppresses EMT and induces apoptosis by downregulating HMGA2 in human colorectal cancer. *J Cell Physiol*, **235**, 920-931.
144. Feng, L., Ma, J., Ji, H., Liu, Y. and Hu, W. (2017) miR-330-5p suppresses glioblastoma cell proliferation and invasiveness through targeting ITGA5. *Biosci Rep*, **37**.
145. Trehoux, S., Lahdaoui, F., Delpu, Y., Renaud, F., Leteurtre, E., Torrisani, J., Jonckheere, N. and Van Seuningen, I. (2015) Micro-RNAs miR-29a and miR-330-5p function as tumor suppressors by targeting the MUC1 mucin in pancreatic cancer cells. *Biochim Biophys Acta*, **1853**, 2392-2403.
146. Chen, F.F., Sun, N., Wang, Y., Xi, H.Y., Yang, Y., Yu, B.Z. and Li, X.J. (2020) miR-212-5p exerts tumor promoter function by regulating the Id3/PI3K/Akt axis in lung adenocarcinoma cells. *J Cell Physiol*, **235**, 7273-7282.
147. Lin, J.F., Zeng, H. and Zhao, J.Q. (2018) MiR-212-5p regulates the proliferation and apoptosis of AML cells through targeting FZD5. *Eur Rev Med Pharmacol Sci*, **22**, 8415-8422.
148. Lv, Z.D., Yang, D.X., Liu, X.P., Jin, L.Y., Wang, X.G., Yang, Z.C., Liu, D., Zhao, J.J., Kong, B., Li, F.N. *et al.* (2017) MiR-212-5p Suppresses the Epithelial-Mesenchymal Transition in Triple-Negative Breast Cancer by Targeting Prrx2. *Cell Physiol Biochem*, **44**, 1785-1795.
149. Li, X., Li, N., Niu, Q., Zhu, H., Wang, Z. and Hou, Q. (2020) Elevated Expression of miR-629 Predicts a Poor Prognosis and Promotes Cell Proliferation, Migration, and Invasion of Osteosarcoma. *Onco Targets Ther*, **13**, 1851-1857.
150. Wang, J., Guo, X.J., Ding, Y.M. and Jiang, J.X. (2017) miR-1181 inhibits invasion and proliferation via STAT3 in pancreatic cancer. *World J Gastroenterol*, **23**, 1594-1601.
151. Zhang, H.Y., Li, J.H., Li, G. and Wang, S.R. (2015) Activation of ARK5/miR-1181/HOXA10 axis promotes epithelial-mesenchymal transition in ovarian cancer. *Oncol Rep*, **34**, 1193-1202.
152. Monteleone, N.J. and Lutz, C.S. (2017) miR-708-5p: a microRNA with emerging roles in cancer. *Oncotarget*, **8**, 71292-71316.
153. Dong, H.T., Liu, Q., Zhao, T., Yao, F., Xu, Y., Chen, B., Wu, Y., Zheng, X., Jin, F., Li, J. *et al.* (2020) Long Non-coding RNA LOXL1-AS1 Drives Breast Cancer Invasion and Metastasis by Antagonizing miR-708-5p Expression and Activity. *Mol Ther Nucleic Acids*, **19**, 696-705.

154. Chen, Q., Xu, H., Zhu, J., Feng, K. and Hu, C. (2020) LncRNA MCM3AP-AS1 promotes breast cancer progression via modulating miR-28-5p/CENPF axis. *Biomed Pharmacother*, **128**, 110289.
155. Zhao, Z. and Qin, X. (2020) MicroRNA-708 targeting ZNF549 regulates colon adenocarcinoma development through PI3K/AKt pathway. *Sci Rep*, **10**, 16729.
156. Yu, Y., Chang, Z., Han, C., Zhuang, L., Zhou, C., Qi, X. and Peng, Z. (2020) Long non-coding RNA MINCR aggravates colon cancer via regulating miR-708-5p-mediated Wnt/beta-catenin pathway. *Biomed Pharmacother*, **129**, 110292.
157. Almeida, M.I., Nicoloso, M.S., Zeng, L., Ivan, C., Spizzo, R., Gafa, R., Xiao, L., Zhang, X., Vannini, I., Fanini, F. *et al.* (2012) Strand-specific miR-28-5p and miR-28-3p have distinct effects in colorectal cancer cells. *Gastroenterology*, **142**, 886-896 e889.
158. Luan, X.F., Wang, L. and Gai, X.F. (2019) The miR-28-5p-CAMTA2 axis regulates colon cancer progression via Wnt/beta-catenin signaling. *J Cell Biochem*.
159. Shi, X. and Teng, F. (2015) Down-regulated miR-28-5p in human hepatocellular carcinoma correlated with tumor proliferation and migration by targeting insulin-like growth factor-1 (IGF-1). *Mol Cell Biochem*, **408**, 283-293.
160. Huang, S., Guo, H., Cao, Y. and Xiong, J. (2019) MiR-708-5p inhibits the progression of pancreatic ductal adenocarcinoma by targeting Sirt3. *Pathol Res Pract*, **215**, 794-800.
161. Fazio, S., Berti, G., Russo, F., Evangelista, M., D'Aurizio, R., Mercatanti, A., Pellegrini, M. and Rizzo, M. (2020) The miR-28-5p Targetome Discovery Identified SREBF2 as One of the Mediators of the miR-28-5p Tumor Suppressor Activity in Prostate Cancer Cells. *Cells*, **9**.
162. Hernandez-Verdun, D. (2011) Assembly and disassembly of the nucleolus during the cell cycle. *Nucleus*, **2**, 189-194.
163. Slack, F.J. and Chinnaiyan, A.M. (2019) The Role of Non-coding RNAs in Oncology. *Cell*, **179**, 1033-1055.
164. Samad, A.F.A. and Kamaroddin, M.F. (2023) Innovative approaches in transforming microRNAs into therapeutic tools. *Wiley Interdiscip Rev RNA*, **14**, e1768.
165. Deng, Y., Campbell, F., Han, K., Theodore, D., Deeg, M., Huang, M., Hamatake, R., Lahiri, S., Chen, S., Horvath, G. *et al.* (2020) Randomized clinical trials towards a single-visit cure for chronic hepatitis C: Oral GSK2878175 and injectable RG-101 in chronic hepatitis C patients and long-acting injectable GSK2878175 in healthy participants. *J Viral Hepat*, **27**, 699-708.
166. Ottosen, S., Parsley, T.B., Yang, L., Zeh, K., van Doorn, L.J., van der Veer, E., Raney, A.K., Hodges, M.R. and Patick, A.K. (2015) In vitro antiviral activity and preclinical and clinical resistance profile of miravirsen, a novel anti-hepatitis C virus therapeutic targeting the human factor miR-122. *Antimicrob Agents Chemother*, **59**, 599-608.